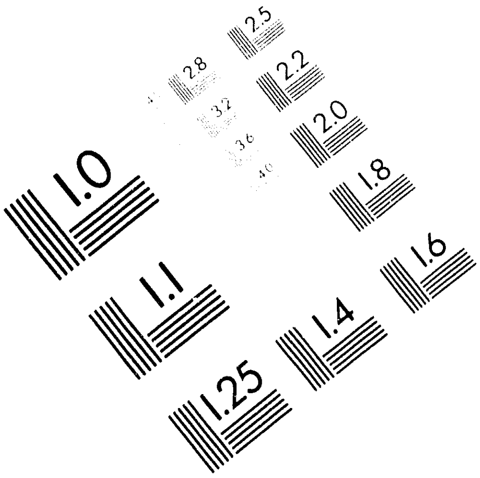

AIIM

Association for Information and Image Management

1100 Wayne Avenue, Suite 1100
Silver Spring, Maryland 20910
301/587-8202

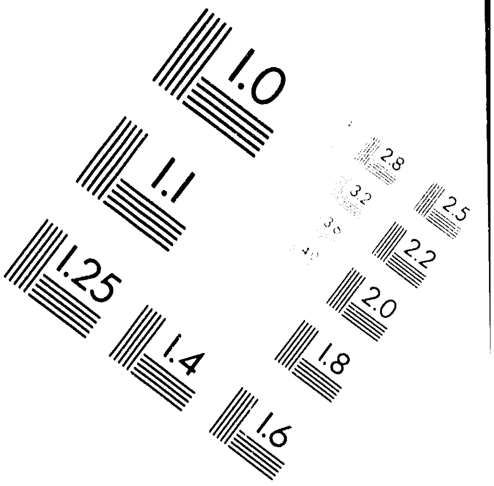

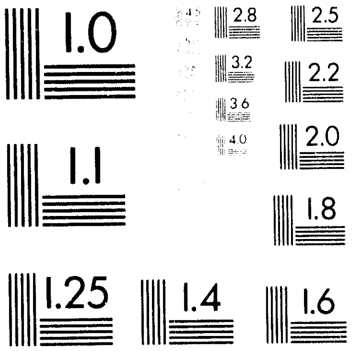

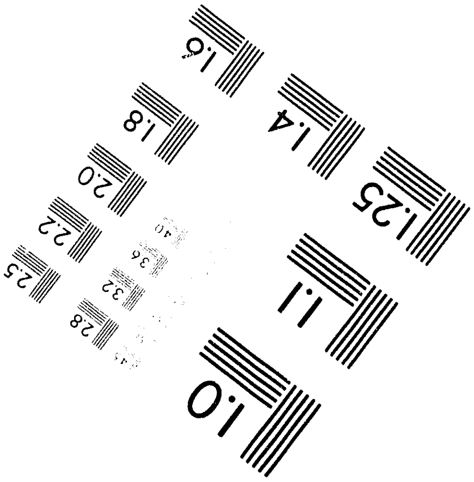

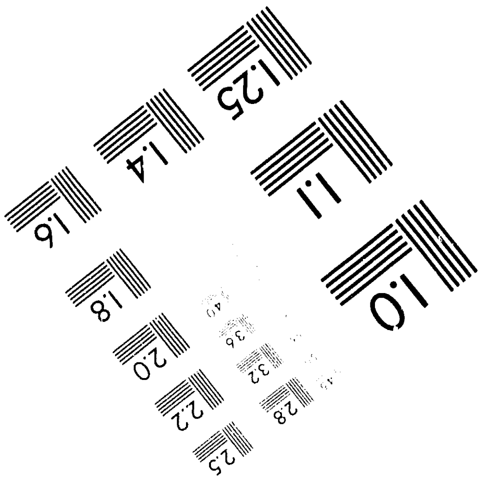

MANUFACTURED TO AIIM STANDARDS
BY APPLIED IMAGE, INC.

1 of 1

SAND94-0694
Unlimited Release
Printed June 1994

Distribution
Category UC-706

Preradiation Studies for Non-Thermal Z-Pinch Wire Load Experiments on Saturn*

T. W. L. Sanford
Intense Beam Research Department

D. R. Humphreys
Target and Analysis Theory Department

J. W. Poukey and B. M. Marder
Beam. Plasma, and Electromagnetic Theory Department

J. A. Halbleib
Simulation Technology Research Department

J. T. Crow and R. B. Spielman
High Energy Plasma Physics Department

Sandia National Laboratories
Albuquerque, NM 87185

R. C. Mock
Ktech Corporation
Albuquerque, NM 87110

Abstract

The implosion dynamics of compact wire arrays on Saturn are explored as a function of wire mass m, wire length ℓ, wire radii R, and radial power-flow feed geometry using the ZORK code. Electron losses and the likelihood of arcing in the radial feed adjacent the wire load are analyzed using the TWOQUICK and CYLTRAN codes. The physical characteristics of the implosion and subsequent thermal radiation production are estimated using the LASNEX code in one dimension. ***These analyses show that compact tungsten wire arrays with parameters suggested by D. Mosher and with a 21-nH vacuum feed geometry satisfy the empirical scaling criterion*** $I/(m/\ell) \sim 2$ ***MA/(mg/cm) of Mosher for optimizing non-thermal radiation from z pinches, generate low electron losses in the radial feeds, and generate electric fields at the insulator stack below the Charlie Martin flashover limit thereby permitting full power to be delivered to the load.*** Under such conditions, peak currents of ~ 5 MA can be delivered to wire loads ~ 20 ns before the driving voltage reverses at the insulator stack, potentially allowing the m = 0 instability to develop with the subsequent emission of non-thermal radiation as predicted by the Mosher model.

---

*This research was supported by the U. S. Department of Energy under contract DE-AC04-94AL85000.

Acknowledgments

We thank J. J. Ramirez, W. Beezhold, and K. M. Matzen for vigorous programmatic support; the Saturn z-pinch team and the Saturn crew for technical support; J. S. deGroot, J. E. Maenchen, T. H. Martin, D. M. McDaniel, and D. Mosher for useful discussions; and J. E. Maenchen, D. Mosher, and T. J. Nash for reviewing and L. O. Peterson for typing this report.

Contents

Figures

Tables

Preradiation Studies for Non-Thermal Z-Pinch Wire Load Experiments on Saturn

I. Introduction

Single-wire z-pinch experiments on Gamble II[1,2] and OWL II[3] show a significant yield of hot x rays. The experiments suggest that the radiation is produced by a non-thermal mechanism. The x-ray spectra measured are consistent with a bremsstrahlung production mechanism, which scales as the square of the wire's atomic number (Z). In such a mechanism, electrons are envisaged to be accelerated to ~ 100 keV energies by the inductive fields generated either along the wire load or within the load across collapsing pinch spots associated with the onset of the sausage instability.

Early Gamble-II data suggest that the condition for maximizing the "run-away" electrons and the associated radiation corresponding to this mechanism is given by the Mosher criterion[1]

$$I/(m/\ell) \sim 2\,\mathrm{MA}/(\mathrm{mg/cm}) \ , \tag{1}$$

where I is the current flowing through the wire load having a mass per unit length of m/ℓ. At this optimum, 60 J of x rays above 15 keV are generated in a 50-µm diameter tungsten wire of 4-cm length on Gamble II operating at 0.8 MA. Assuming that this radiation scales like I^2 (as is measured for copper K-shell x rays on Gamble II, Double Eagle, and Saturn),[1] then 340 kJ of x rays greater than 15 keV are expected for the 60-MA Jupiter accelerator. This yield is sufficient to satisfy the Jupiter testing needs in this hot x-ray energy band. Accordingly, a series of experiments on the 10-MA Saturn accelerator[4] are being conducted to validate these scaling expectations and to understand the basic physics mechanisms behind the production of hot x rays.

Saturn, however, is a low-impedance, low-inductance electron accelerator. As such, it is prone to flashover of its Lucite insulator stack (Fig. 1A) at the vacuum-water interface due to the high inductive voltage drop generated when the accelerator quickly drives a high-inductance load, as would be the case for a single wire load mounted on axis. Thus, the rapid implosion of compact wire arrays instead of a single exploding wire on axis has been proposed by Mosher[1] for the Saturn experiments. In this arrangement, the initial inductance of the wire array is kept low, preventing insulator flashover early in the current pulse. The radius of the wire array is chosen such that the implosion occurs early with respect to the time of peak current, enabling the wires to form a single axial slug and permitting the sausage instability to be well established during the peak portion of the pulse. Alternatively, a single exploding wire on axis enclosed by a set of robust, high-mass cathode current posts to reduce the overall inductance of the load could be used. Calculations show, however, that this arrangement does not produce sufficient current to the axial wire for practical geometries (Appendix A, Section VI) and is not considered further here.

Calculations show that compact wire arrays of 2-mm radius, 2-cm length, and ~ 5-mg mass meet the Mosher criterion (Eq. 1) on Saturn. This mass, however, is an order of magnitude smaller than that which maximizes the kinetic energy (KE) given the wire array during the implosion phase and which would optimize the thermal radiation if the load wire were operating as a conventional plasma-radiation-source. In this report, we first examine the dynamics of the implosions of wire arrays throughout this mass range in

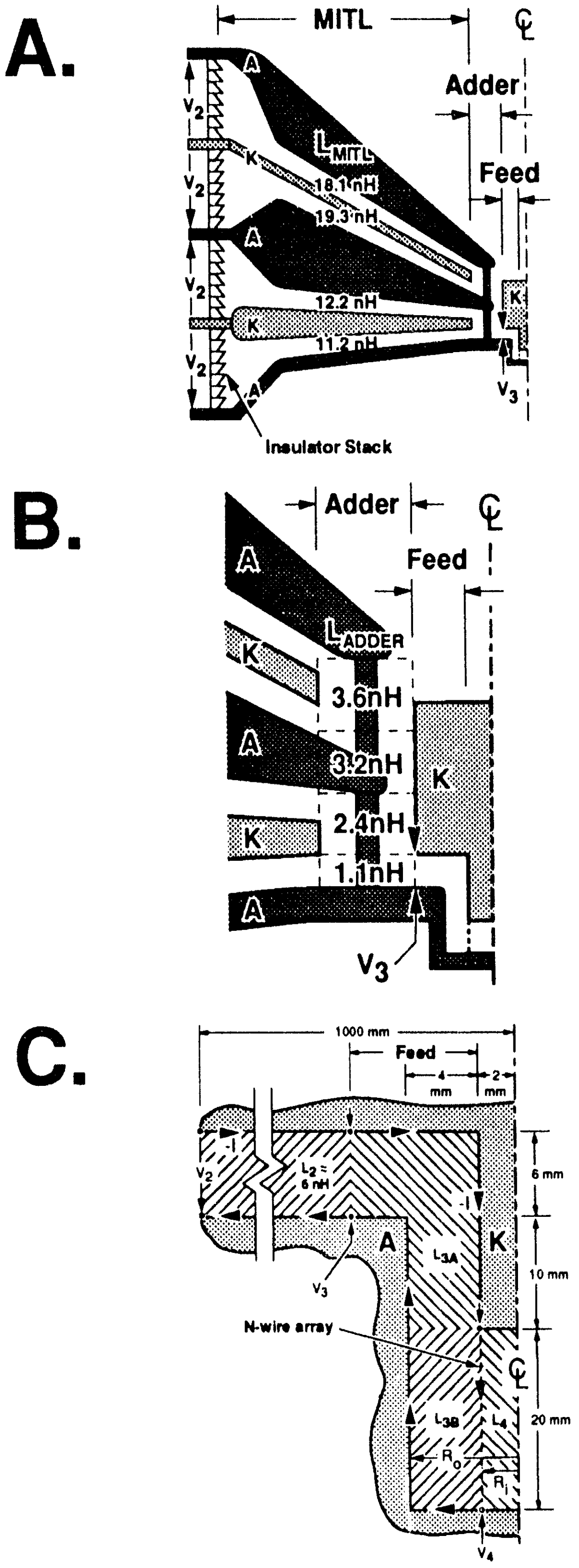

Figure 1. Schematic of Saturn vacuum power flow sections showing (A) an overview, (B) detail of adder section, and (C) detail of idealized feed section.

relation to the circuit parameters of the Saturn accelerator using the idealized geometry of Fig. 1C. Specifically, we examine in detail the conditions under which the Mosher criterion is satisfied, when the maximum KE is given the load, and the conditions under which the insulator may flashover. The numerical tool used in this analysis is the modified circuit/implosion code ZORK.[5]

For two masses, one that satisfies the Mosher criterion and one that optimizes the KE given the load, the physical characteristics of the implosion are next examined using the one-dimensional (1D) LASNEX code[6] for tungsten loads. In this configuration, LASNEX is a one-fluid, magneto-hydrodynamic (MHD) code having three temperatures corresponding to that of the resulting plasma ions, electrons, and photons. It is used to confirm the implosion dynamics of the revised ZORK code, and importantly to give insight into the current and charge densities, the magnetic and electric fields, and the particle temperatures generated during the implosion phase for tungsten loads. It enables the resistance of the load, which is ignored in ZORK, and the thermal radiation to be estimated and provides a starting point for calculations of the non-thermal mechanisms.

In the radial magnetically-insulated-transmission-line (MITL) that feeds power to the load, electrons may be lost to the anode near the load. If the energy deposition from these loss electrons is high enough, an anode plasma may form, resulting in arcing between the cathode and anode, reducing current to the load. In the last section of this report, this loss mechanism and subsequent energy deposition in the anode is examined with the 2D TWOQUICK[7] and CYLTRAN[8,9] codes, respectively, and is compared with depositions necessary to initiate an anode plasma. TWOQUICK is an electromagnetic particle-in-cell (PIC) code, which generates the electron distributions that are used as input by CYLTRAN. CYLTRAN is an electron/photon Monte Carlo transport code that in turn is used to calculate the subsequent energy deposition at the anode surface.

II. Implosion Dynamics

A. Equivalent Circuit and ZORK Description

On Saturn, power in the vacuum section is fed to the load using four of the six available MITLs (Fig. 1). Power from the four MITLs is added using a post-hole convolute geometry (Fig. 1B) and is supplied to the load in a single radial feed (Fig. 1C). Because the transit times within the vacuum section (< 3 ns) are short relative to the risetime (~ 40 ns) of the current pulse, the current flow within the accelerator can be evaluated using the equivalent circuit of Fig. 2. In Fig. 2, Node 2 represents the position of the vacuum/water interface, L_2 corresponds to the total parallel/series inductance (6 nH) of the combined MITLs and adder (convolute), L_3 is the inductance of the radial feed up to the wire load (which varies between 6 to 18 nH for the geometries considered here), and L_4 represents the inductance of the plasma wire load and is given approximately by:

$$L_4(t) \sim 2\ell \ \ln R_i/R(t) \quad . \tag{2}$$

Here R_i represents the initial radius of the wire array (typically 0.2 cm) and R(t), the reduced radius after time t (Fig. 3). ℓ is in units of cm and L is in units of nH. Outside the vacuum section, the accelerator is represented by the open circuit voltage V(t) in series with a 1/6-ohm impedance Z and a 0.75-nH inductor L_1. For all calculations presented in this report, V(t) used is that inferred from voltage measurements[10] made on a single water triplate transmission line and is shown as V_{in} in Fig. 4.

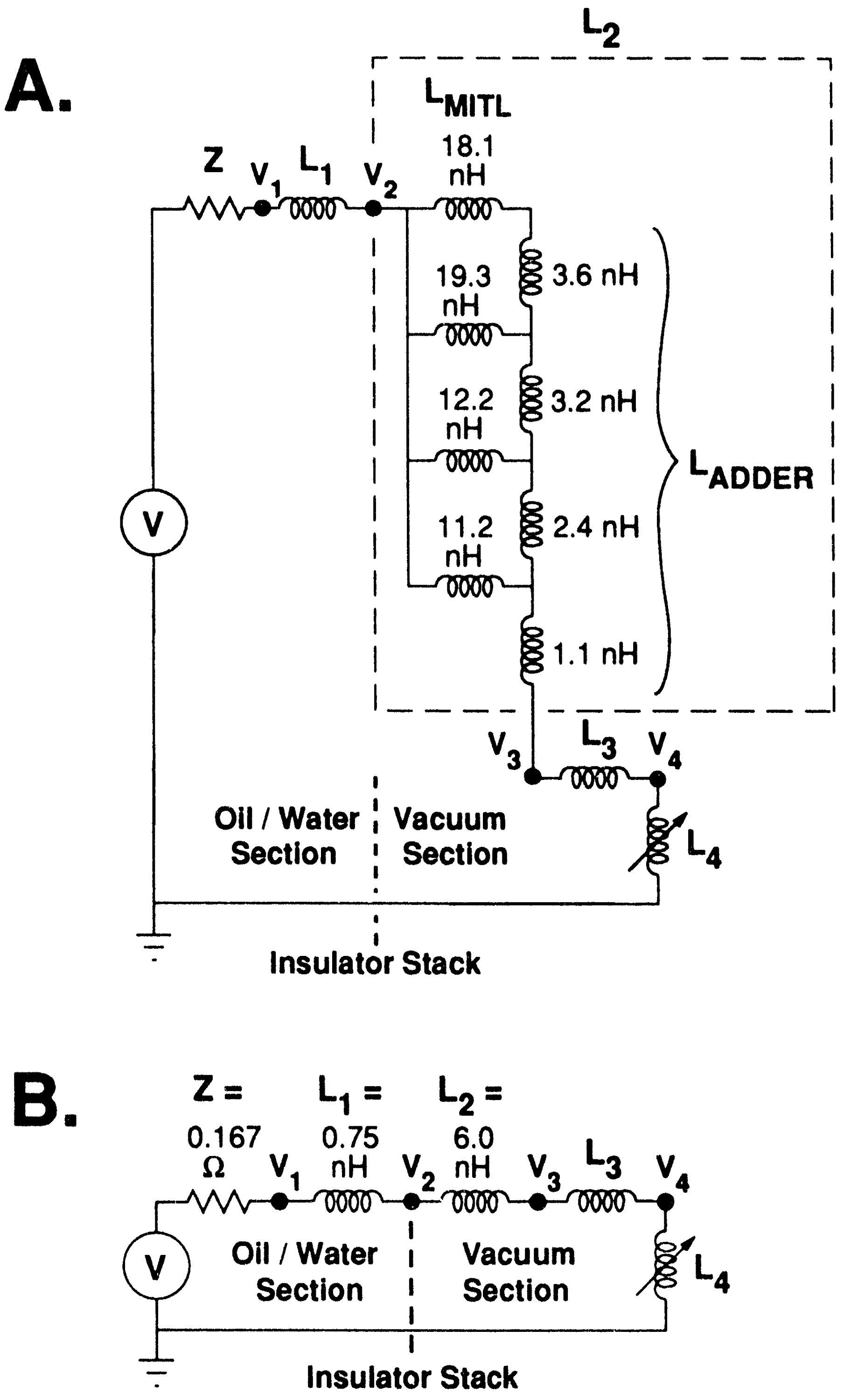

Figure 2. Equivalent circuit of Saturn (A) corresponding to inductances shown in Figs. 1A and 1B and (B) used in ZORK calculations.

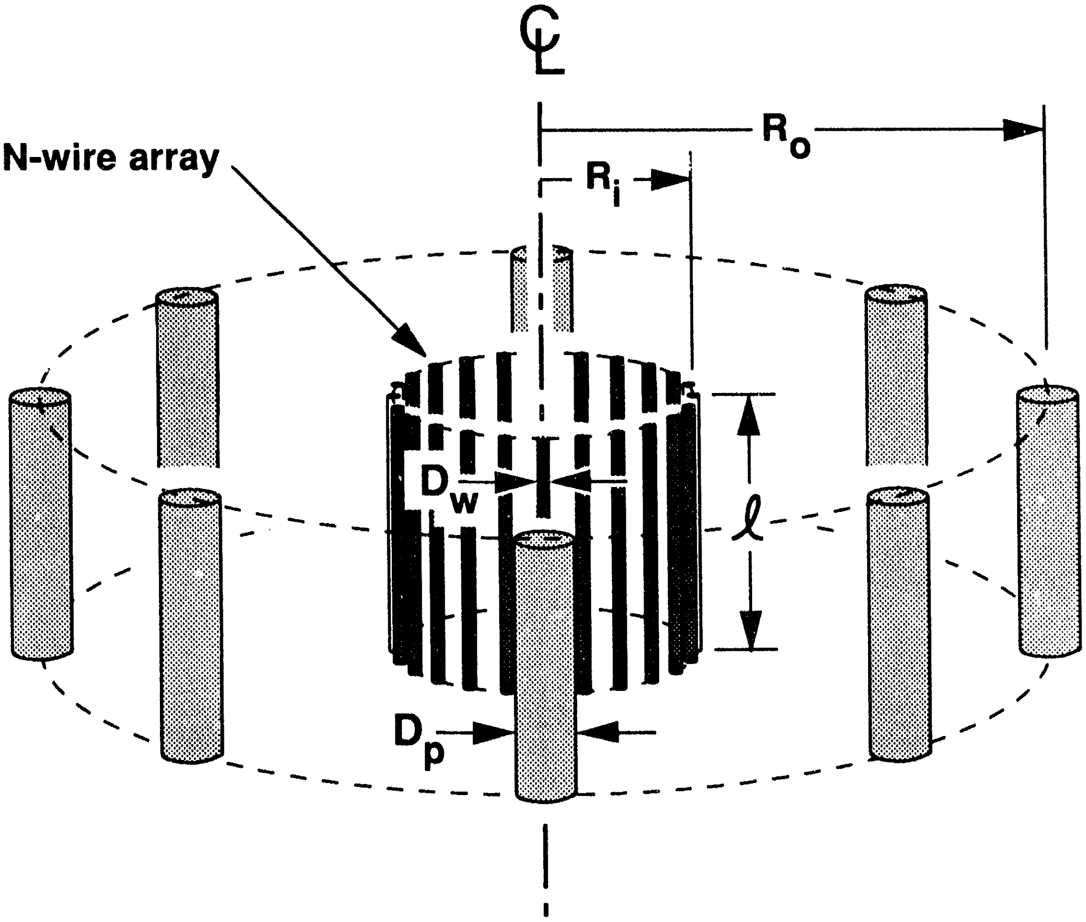

Figure 3. Realistic load showing the radial/azimuthal structure of the compact wire array (having initial radius R_i) with respect to the anode current return posts at radius R_0.

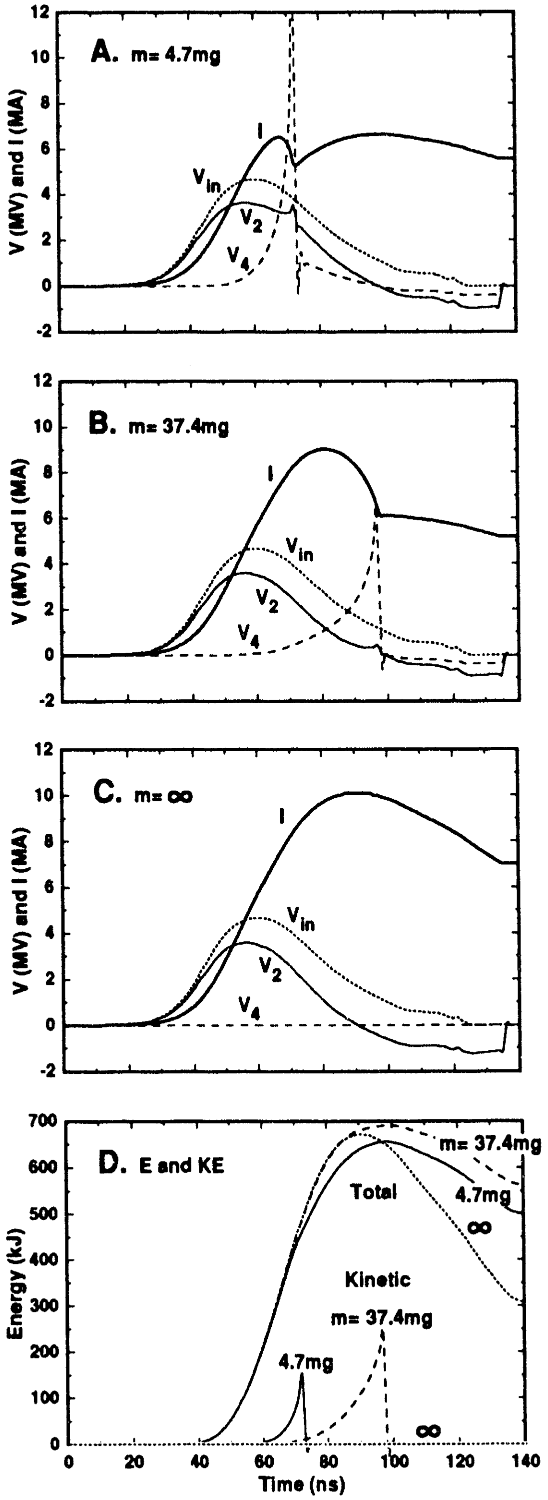

Figure 4. Voltage and current waveforms for the geometry of Fig. 1C and circuit of Fig. 2 when (A) m = 4.7 mg, (B) m = 37.4 mg, and (C) m = ∞, and (D) corresponding total system energy and KE given the load. For these calculations $\ell = 2$ cm, $R_0 - R_i = 4$ mm, and $L_2 + L_3 = 12.4$ nH.

In ZORK, the current flowing in the load is found by simultaneously solving the circuit equation associated with Fig. 2B,

$$V(t) = ZI + (L_1 + L_2 + L_3)\frac{dI}{dt} + \frac{d}{dt}(L_4 I) \ , \tag{3}$$

and Newton's first law of motion of the imploding wire array taken to be a thin-wall cylinder of total mass m (Fig. 3),

$$\frac{m\, d^2R}{dt^2} = 2\pi R\ell \left(\frac{B^2}{2\mu_0}\right) \tag{4}$$

$$\mu_0 = 4\pi \ 10^{-7} \ \text{H/m} \, .$$

Here, the term in brackets is the magnetic pressure per unit area from the current I flowing through the wires, and the magnetic field B at R is obtained from Ampere's circuital law,

$$B = \frac{\mu_0 I}{2\pi R} \ , \tag{5}$$

all in SI units.

The actual Saturn anode load hardware surrounding the wire array consists of a set of large diameter current return posts symmetrically placed about the axis of the accelerator, which permits the radiation generated from the implosion to escape the load region (Fig. 3). This structure as well as the finite nature of the wire array slightly increases the inductance of the load over that estimated in ZORK using Eq. 2. This approximation is discussed in Appendix B, Section VI.

The original ZORK code has been revised (1) to enable the voltage waveform V(t) to be read in without reference to UFO subroutines, (2) to enable the radius of the imploding load to remain fixed at a given implosion radius once that radius is reached, and (3) to enable the electric fields relative to the Charlie Martin (CM) insulator flashover limits[11] and the magnetic flashover inhibition (MFI) limit[12] to be estimated. The CM limit states that to prevent flashover, the electric field E at the stack should remain below E_{cm}, given by

$$E_{cm} = 175 \ t^{-1/6} A^{-1/10} \ . \tag{6}$$

Here E, t, and A are in units of kV/cm, μs, and cm^2, respectively. A represents the cylindrical area of the stack of radius r between a given MITL of height h. For Saturn, r = 100 cm, h ~ 31 cm, and A ~ 1.95×10^4 cm^2. The variable t corresponds to the full-width half-maximum (FWHM) of the 6th power of the voltage pulse across the stack and is 0.016 μs for Saturn pulses. Ignoring the variations among the four MITLs, the CM limit for Saturn is thus 130 kV/cm. If this limit is exceeded, the time of breakdown is estimated in ZORK by asking when the time integral of E^6 exceeds $175^6/A^{6/10}$ (Ref. 13):

$$\int_0^t E^6 dt = \frac{175^6}{A^{6/10}} . \qquad (7)$$

By taking advantage of **ExB** drift effects of the electrons born at the insulator stack that initiate the flashover process, these limits can be exceeded. If the magnetic fields generated at the stack from the current flowing in the given MITL enables the relation (SI units),

$$E/cB < 0.09 , \qquad (8)$$

to be satisfied, then the insulator will not flash.[13] Unfortunately, for most of the geometries considered in this report, this limit is exceeded, so that MFI is not a significant help in circumventing the CM limit.

The implosion dynamics of the revised ZORK code have been checked against LASNEX using the idealized geometry of Fig. 1C for a tungsten load where $R_i = 0.2$ cm, $\ell = 2$ cm, $m = 4.7$ mg, and $L_2 + L_3 = 12.4$ nH. The comparison between that calculated by ZORK and LASNEX shown in Fig. 5 of the radial position R (Fig. 5A) and velocity v (Fig. 5B) of the wire annulus and of the load current I (Fig. 5C) up to the time of assembly on axis (where the ZORK calculation ends) is excellent. The comparison gives confidence in the revised ZORK and the approximation used in ZORK of neglecting the resistance of the load, which is included in the LASNEX calculation. The comparison also illustrates the global features of the implosion process (discussed also in Ref. 14): as the radius contracts, particularly during the final phase of the implosion, the inductance of the load rapidly increases, reducing the load current. In LASNEX, once the wires have assembled on axis, the wires' inward momentum is reversed with the load expanding and contracting in response to magnetic pressure. Details of the characteristics of the resulting plasma such as temperature and density are discussed in the next section.

As a last point on the validity and relevance of the ZORK analyses, we have compared ZORK predictions with Saturn Shot 1742 in Fig. 6. This shot used a krypton gas-puff load with an outside radius of 2.28 cm, an inside radius of 1.28 cm, $\ell = 2$ cm, $m = 0.4$ mg, and $L_2 + L_3 = 9.3$ nH. In Fig. 6, ROGO corresponds to an average of the Rogowski coil monitors located at the insulator stack (i.e., near Node 2 in Fig. 2), and IPIEZ and IBDOT correspond to a piezoelectric pressure gauge and $\dot{B}$ monitor, respectively, each located 5-cm outside the load (i.e., between Nodes 3 and 4 in Fig. 2). In the comparison, the measurements are time shifted and scaled (values noted) such that the peak values approximately coincide. While the comparison is reasonable, this does illustrate either the limitations of ZORK in predicting the load dynamics or the measurement fidelity. The differences between the predicted and measured current risetimes is likely due to variations among the four MITL current pulses driving the load. The comparison suggests a 17-ns root-mean-square (RMS) jitter, which is consistent with previous measurements.

B. Dynamics versus Load Mass

We now turn to the variation in the circuit parameters calculated by ZORK as a function of the wire-array-mass m up to the time of implosion, for the idealized geometry of Fig. 1C. In this report, implosion refers to that point in time when the radius has typically contracted by a factor of ten to a radius of 200 μm, unless otherwise stated.

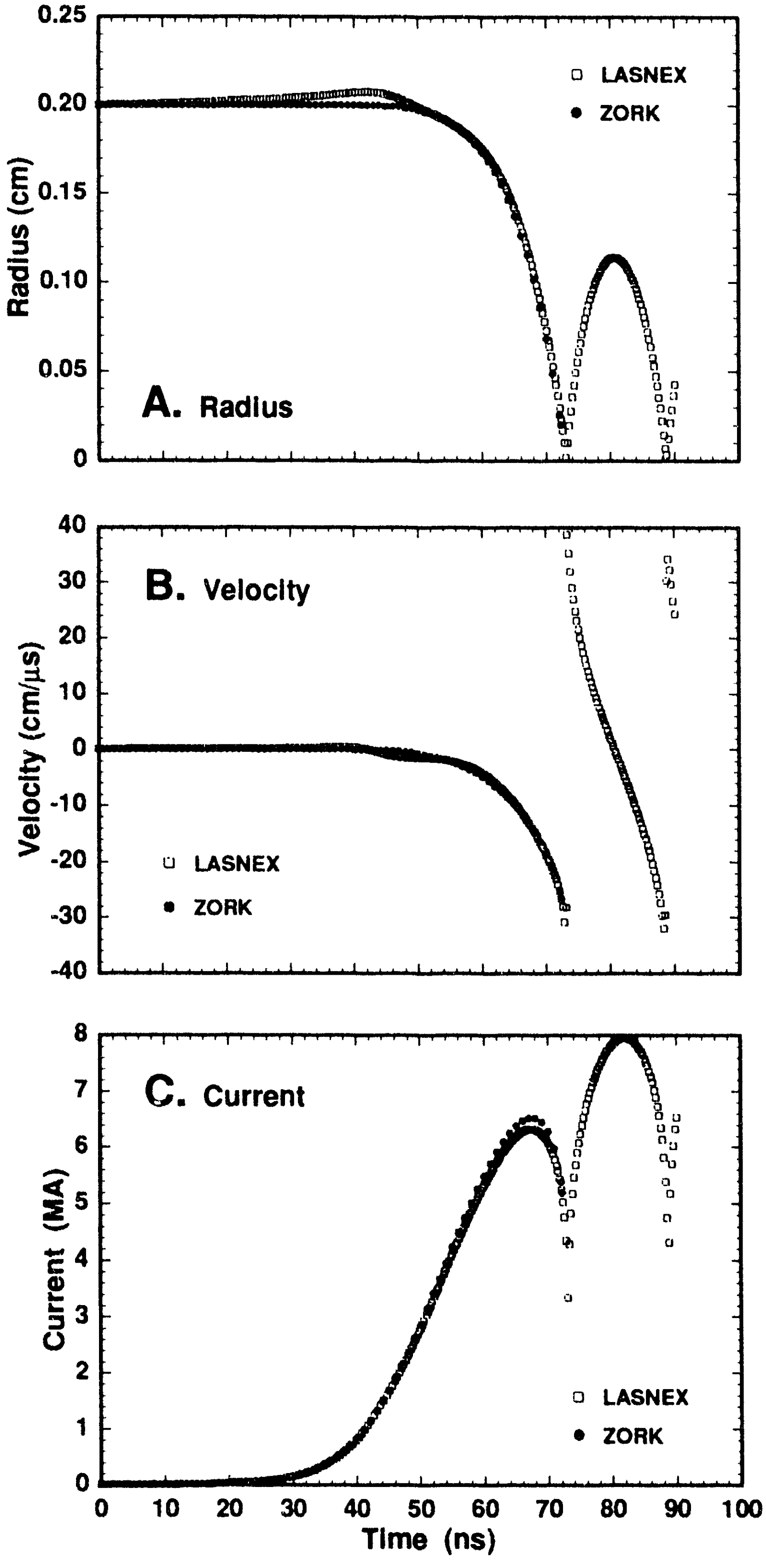

Figure 5. Comparison of LASNEX and ZORK calculations of (A) radius, (B) velocity, and (C) current during the implosion for the conditions of Fig. 4A.

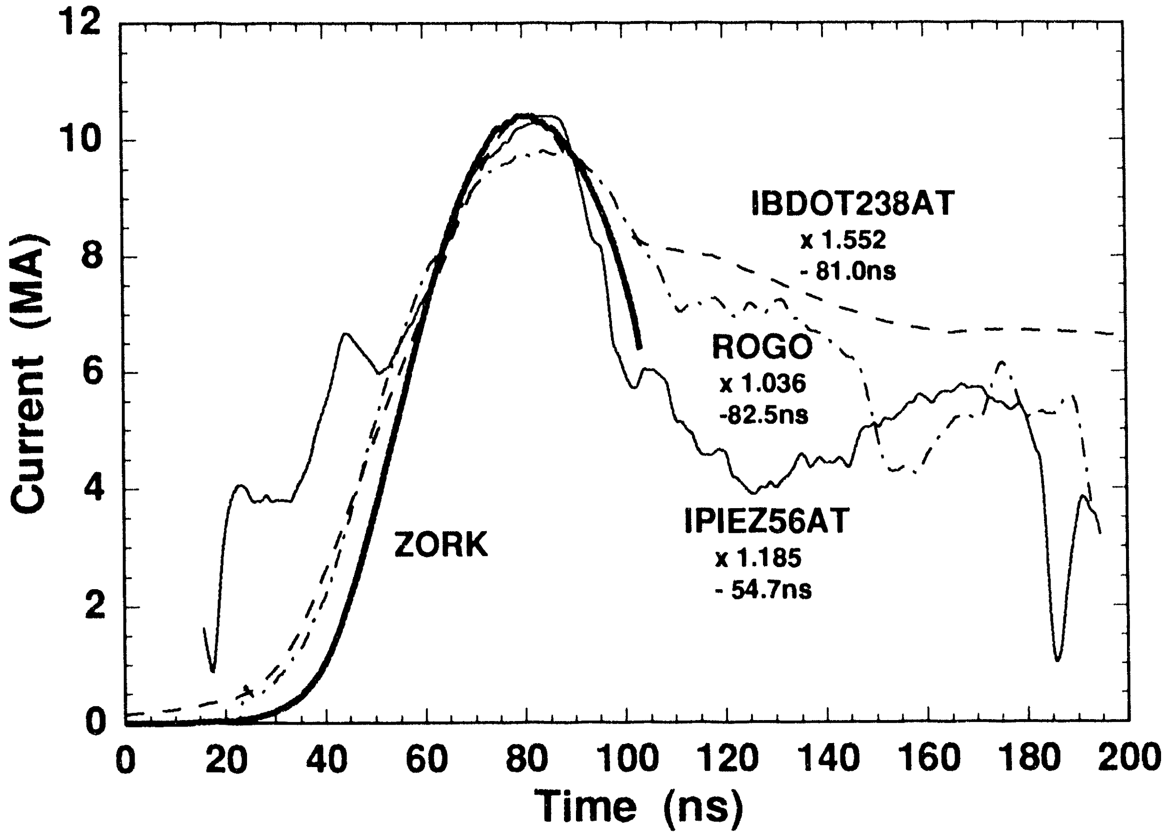

Figure 6. Comparison of measured current waveforms with that calculated by ZORK for Shot 1742. See text for monitor and shot description.

As the mass increases, the length of time to reach implosion (Fig. 7A) or peak current in the load (Fig. 7B) increases, the maximum current during implosion (Fig. 7C) increases, and the velocity at implosion (Fig. 7D) decreases, as expected from Eq. 4. The increase in current follows from the reduced time rate of change of the load inductance associated with the slower moving array.

Figure 4 shows the input voltage V_{in}, and the voltages across the insulator stack (Node 2 in Fig. 2A) and across the wire array (Node 4) for three different masses within the range of masses explored. Figure 4C corresponds to an infinite mass array, namely one that remains stationary. The L/R risetime of the equivalent circuit is 79 ns. The peak current (Fig. 7C) of 10 MA occurs ~ 90 ns (Fig. 7B) after initiation of the applied voltage and corresponds to the time when the voltage reverses at the insulator stack and power begins to cycle out of the load (wire array).

By contrast, Fig. 4A corresponds to the associated waveforms for the low mass array used for Fig. 5, which satisfies the Mosher criterion (Eq. 1) at the implosion radius of 200 μm (Fig. 7E). In this ZORK calculation, as compared with that shown in Fig. 5, once the array contracts by a factor of 10 to the radius of 200 μm, the radius is held fixed and the circuit calculation is allowed to continue enabling the general characteristics of

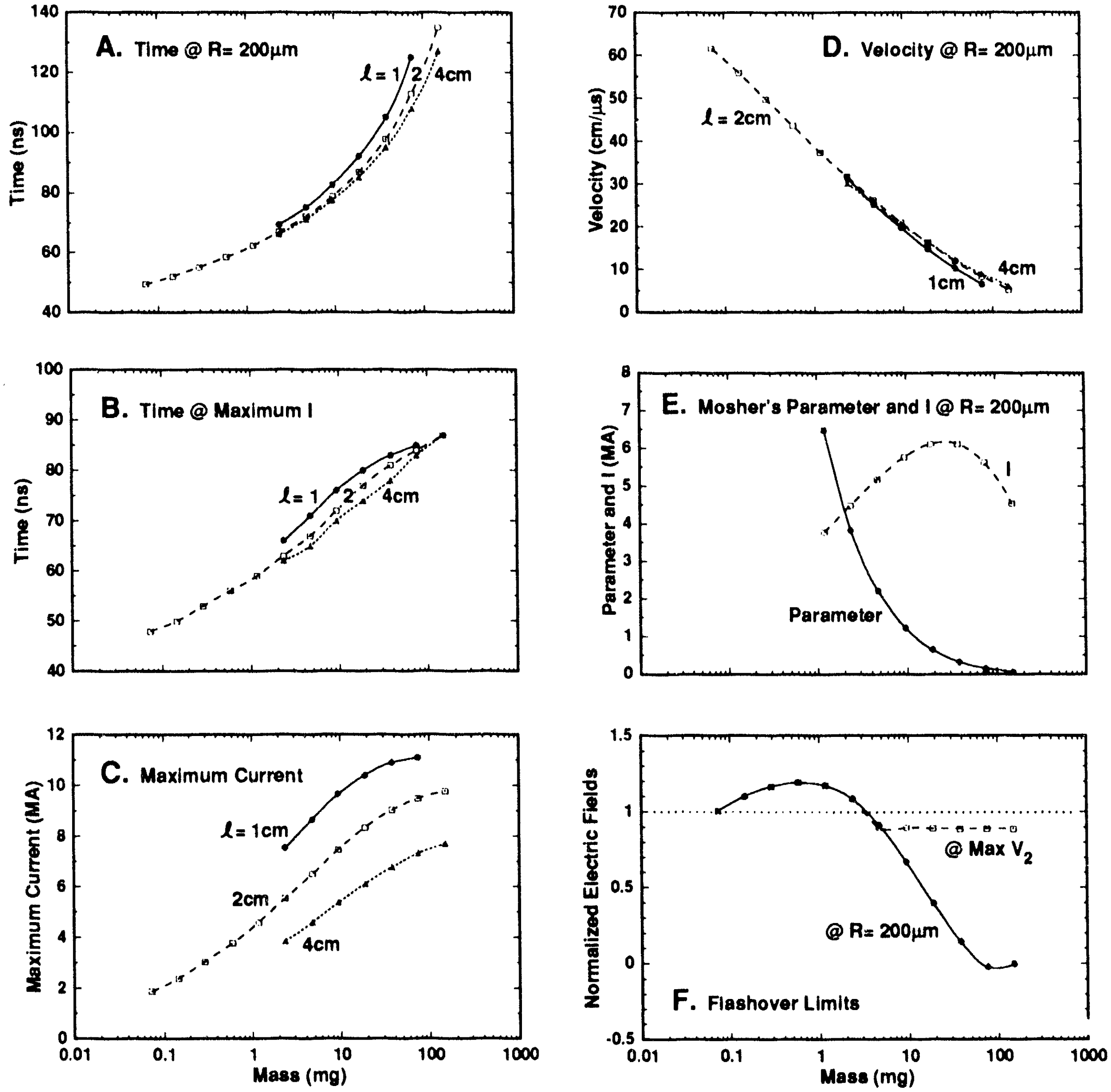

Figure 7. Comparison of (A) implosion times, (B) times of maximum current during the implosion, (C) the maximum current flowing during the implosion, (D) velocity at implosion, (E) the Mosher parameter [I/(m/ℓ)] (see Eq. 1) and current flowing at implosion, and (F) the electric fields at the insulator stack normalized by the CM limit (Eq. 6) at maximum stack voltage and at implosion as a function of load mass and length. Geometry and circuit corresponds to that of Figs. 1C and 2B, respectively, with $L_2 + L_{3A} = 8$ nH and $R_0 - R_i = 4$ mm.

the waveforms to be estimated after implosion is reached. Because the power continues to be driven toward the load after implosion, the current rises again once the radial contraction has stopped. In this model, the magnitude of the current rise after implosion has the potential for providing insight to the radial extent of the implosion as illustrated in Fig. 8, where the final implosion radius is varied between 50 and 1900 μm.

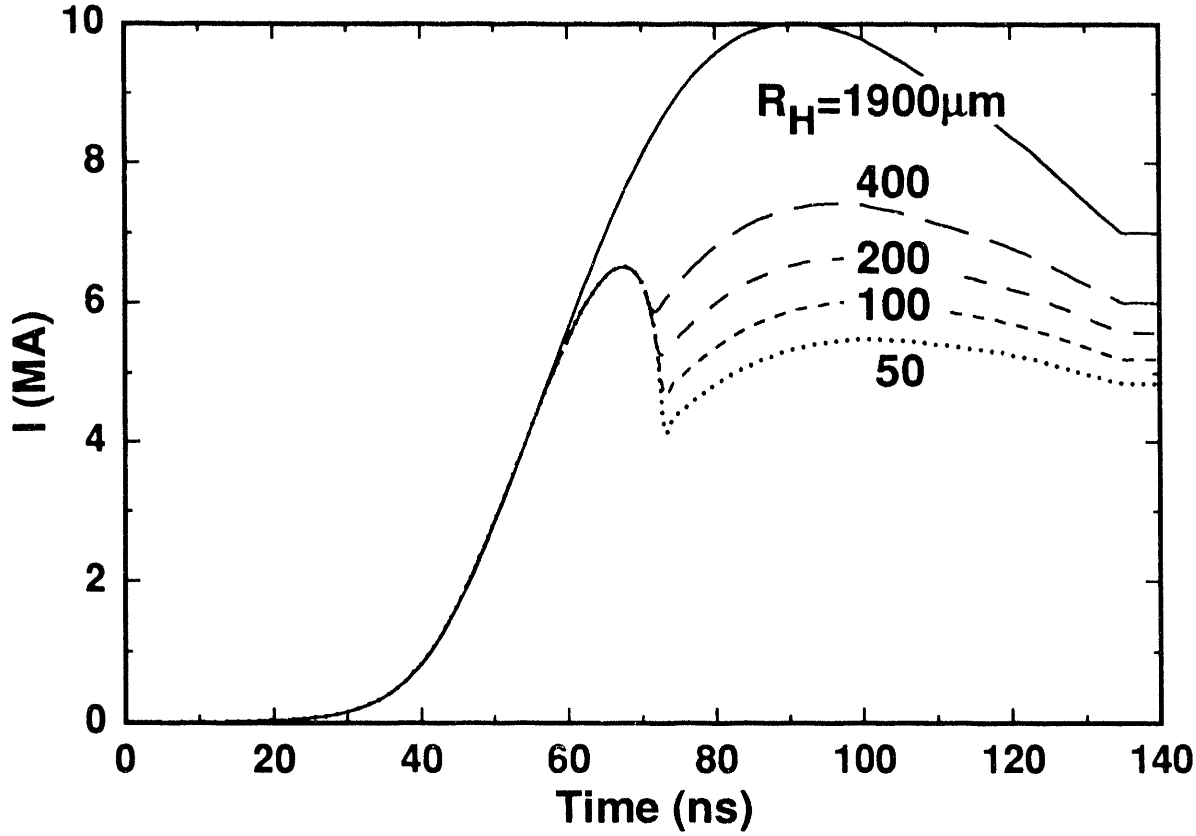

Figure 8. Comparison of current wave shapes as a function of final implosion radii R_H. R_H is held fixed, once R_H is reached. Conditions correspond to those of Fig. 4A.

As the final implosion radius is approached (Fig. 5A), the load inductance changes rapidly, and the voltage V_4 across the load rises markedly (Eq. 3), resulting in a corresponding increase in voltage V_2 back at the insulator stack (Fig. 4A). If V_2 is too large, the stack will flash and the maximum current running through the load will be limited to that at the time of flashover. The magnitude of V_4 just after implosion (where the radius now remains stationary) compared with that just prior to implosion shows that the bulk of the voltage rise is due to the rapid change in the load inductance near implosion (assembly).

The electric fields relative to the CM flashover limit (Eq. 6) at the insulator stack are plotted in Fig. 7F as a function of mass for two times within the voltage pulse. One corresponds to the time of maximum V_2 and the other corresponds to the time of implosion. For masses above 5 mg, the implosion is slow enough that the peak field occurs near the time of the peak injected voltage. For lower masses, where a significant voltage is developed across the load, however, the maximum field occurs at the time of implosion. The reduction in peak field for very low masses arises because the implosion is so rapid that little voltage is developed across the insulator stack. For this geometry, only for masses between 0.07 and 3 mg is the CM limit exceeded and then only at the time of implosion.

Adjusting the mass such that the time of implosion occurs just as V_2 reverses at the stack generates the maximum current through the load at implosion and enables the maximum KE to be transferred to the load via the magnetic pinching force (Eq. 4). This condition occurs for a mass of ~ 37 mg. Figure 4B shows the associated current and voltage waveforms at this mass. Figures 9A and 9B show the variation in the current and KE imparted to the load at implosion as a function of mass, respectively.

The time dependence of the KE imparted to the load relative to the total energy in the circuit, for the three mass used in Figs. 4A, B, and C, is shown in Fig. 4D. Note that for the infinite mass case (Fig. 4C) no KE is imparted to the load because the load remains motionless. Qualitatively, the optimum at 37 mg shown in Figs. 8 and 9 is easy to understand. For this mass, the implosion occurs when the system (circuit excluding the voltage driver) is of maximum energy (Fig. 9C). For lower mass (as shown in Fig. 4A), the implosion is reached before all the energy that is available can be extracted. For higher mass (as shown in Fig. 4C), the implosion is so slow that little energy is extracted before the driving pulse is finished.

C. Dynamics versus Load Length

Increasing the length ℓ of the load increases the inductances L_{3B} (Fig. 1C) and L_4 (Eq. 2 and Fig. 3), which results in reduced current flow. Figure 9A shows the reduction in current at the time of implosion (R = 200 μm) when ℓ is increased from 1 to 2 to 4 cm, as a function of mass. Figure 7C shows the associated reduction in the maximum current flowing during the implosion process. Note that for the short 1-cm length, this maximum can exceed 11 MA.

The KE given the load at implosion for these three lengths as a function of mass is shown in Fig. 9B. For these lengths, the maximum KE transferred occurs at a mass per unit length of ~ 10 mg/cm and is approximately independent of length as expected from Eq. 4. Moreover, with increasing length the KE transferred increases monotonically for large masses, with the velocity tracking the square root of the KE (Fig. 7D). This increase is a consequence of energy conservation considerations, which show that the KE transfer efficiency is proportional to the change in the load inductance relative to the total inductance of the system at the end of the implosion process.[15] In general, the KE given the load is linearly proportional to the change in inductance and quadradically proportional to the current at implosion. For the geometry of Fig. 1C at high mass, the effect of the increase in load inductance L_4 offsets the effect of reduced current with increasing ℓ so that the KE transfer increases with increasing length over the range studied. The associated implosion times and time of maximum peak current are given in Figs. 7A and 7B, respectively.

D. Dynamics versus Load Radius

Increasing the initial radius R_i of the wire array (Fig. 3) lengthens the implosion time and lowers the load inductance. Figure 10 illustrates the characteristics of the implosion parameters as R_i is increased from 1 to 10 mm, when

$m = 4.7$ mg,
$\ell = 2$ cm,
$L_2 + L_{3A} = 8$ nH (Fig. 1C), and
$R_0 - R_i = 4$ mm (Fig. 3),

that is, when the radial spacing between the cathode wire array and anode return is fixed at 4 mm. Shown in Fig. 10 are

A. a comparison between the maximum current I_{max} occurring during implosion and that at implosion,

B. a comparison between the time of I_{max} and that of the implosion,

C. a comparison of the starting radius R_i with that at I_{max}, and

D. the KE and velocity at implosion.

This analysis shows, in agreement with Fig. 5A, that relative to the radius at the start of the current pulse, the radius contracts only a small amount, typically 1 to 2 mm before I_{max} is reached. In analogy to the increase in current (Fig. 7C and 9A) and KE (Fig. 9B) transferred to the load with increasing mass when R_i was held fixed, increasing R_i for fixed m increases the current (Fig. 10A) and KE (Fig. 10D) transferred to the load. For $m = 4.7$ mg, the maximum KE transfer occurs when $R_i \sim 7.5$ mm. For larger radii, the KE decreases because (as in the case of very large mass) the implosion time (Fig. 10B) exceeds the time of maximum energy within the system. Interestingly, with $R_i = 2$ mm (which closely satisfies the Mosher criterion [Eq. 1]), by doubling R_i from 2 to 4 mm, I_{max} is increased by ~ 30% and the current at implosion is increased by ~ 10% (Fig. 10A), owing to the lower inductance.

On the other hand, reducing the radius R_i increases the inductance, increasing the voltage within the system and increasing the electric field strength at the insulator stack. Figure 11A compares the peak electric field at the insulator normalized by the CM limit (Eq. 6) with the CM integral over the current pulse normalized by $175^6/A^{6/10}$ (Eq. 7) as a function of R_i. In the calculations R_i is held fixed for the duration of the pulse and R_0 is set to 6 mm as shown in Fig. 1C. The corresponding inductance of the load and maximum current flowing is shown in Fig. 11B. The results of Fig. 11 show that for radii R_i less than ~ 200 μm, the CM limits are exceeded and that flashover is probable. The data indicate that breakdown occurs when the total inductance of the vacuum system up to the wire array exceeds ~ 26 nH. Figure 11B also plots the current reached when the CM integral exceeds $175^6/A^{6/10}$ (Eq. 7).

This analysis shows that breakdown is indeed likely for small radius wires on axis and shows that for such cases, the current that can be driven through the wires is limited to only a few MAs. This observation is the primary reason why the compact wire array geometry with radii on the order of 2 mm were proposed by Mosher for the non-thermal source as discussed in the introduction.

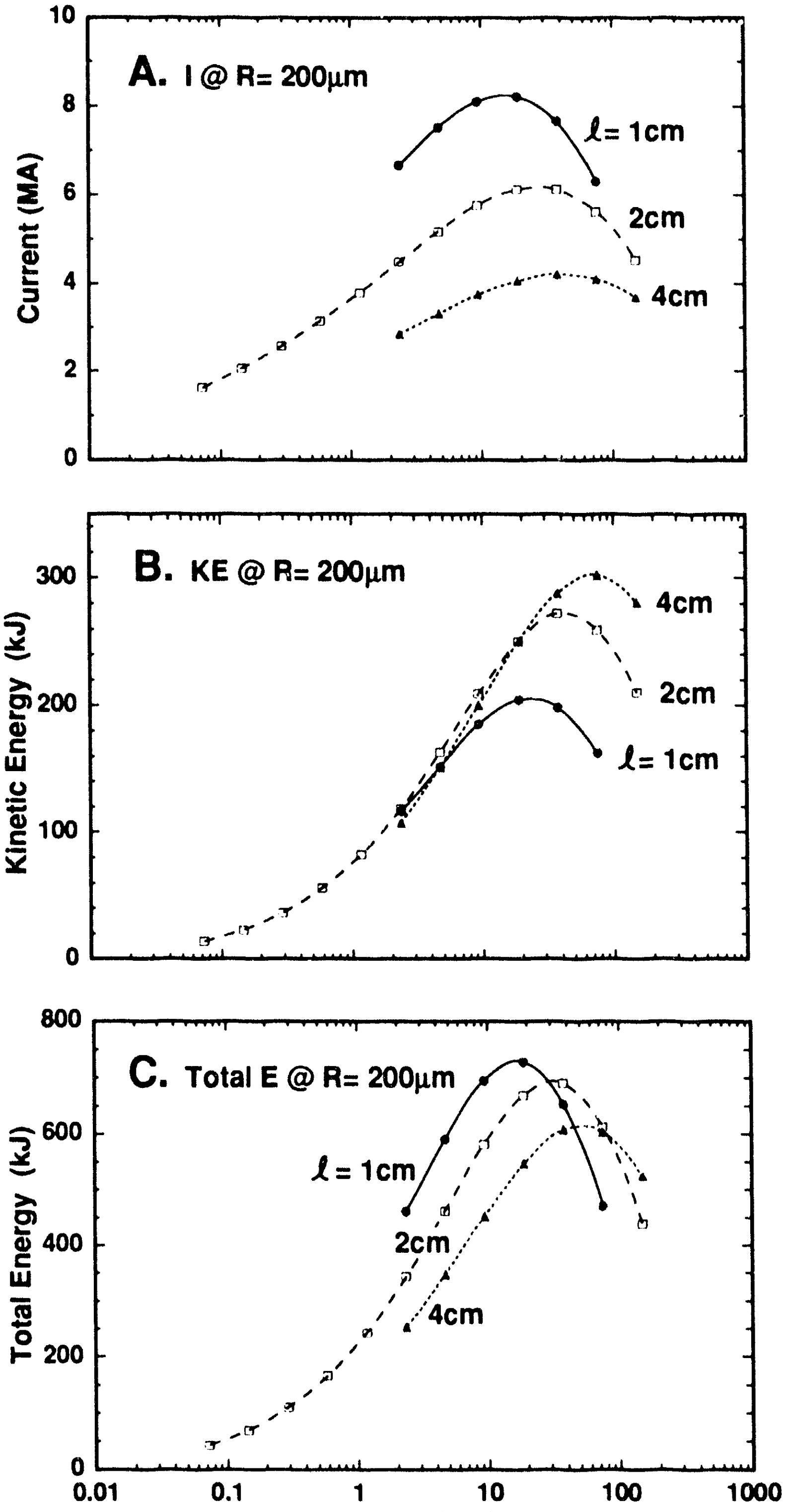

Figure 9. Comparison of (A) current at implosion, (B) KE transferred to the load at implosion, and (C) the total system energy at implosion as a function of load mass and length. Conditions are similar to those of Fig. 4 where $L_2 + L_{3A} = 8$ nH and $R_0 - R_i = 4$ mm.

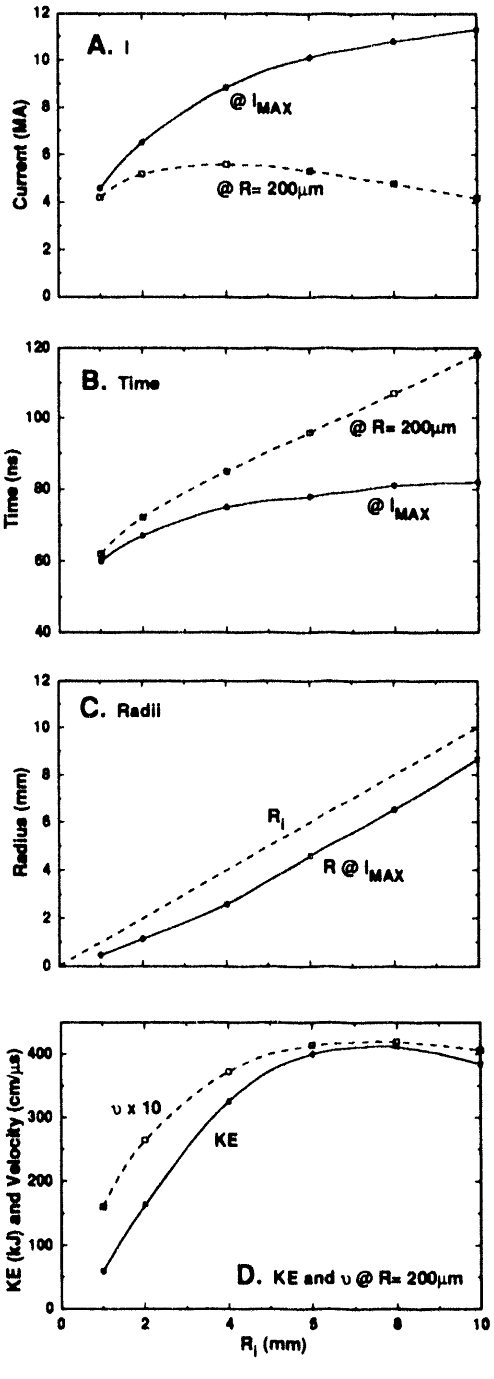

Figure 10. Comparison of (A) maximum current and current at implosion, (B) times of maximum current and implosion, (C) initial radii and radii at maximum current, and (D) KE transferred to the load and velocity at implosion as a function of the initial radius R_i. Geometry and circuit corresponds to that of Figs. 1C and 2B, respectively, with $\ell = 2$ cm, $L_2 + L_{3A} = 8$ nH, and $R_0 - R_i = 4$ mm.

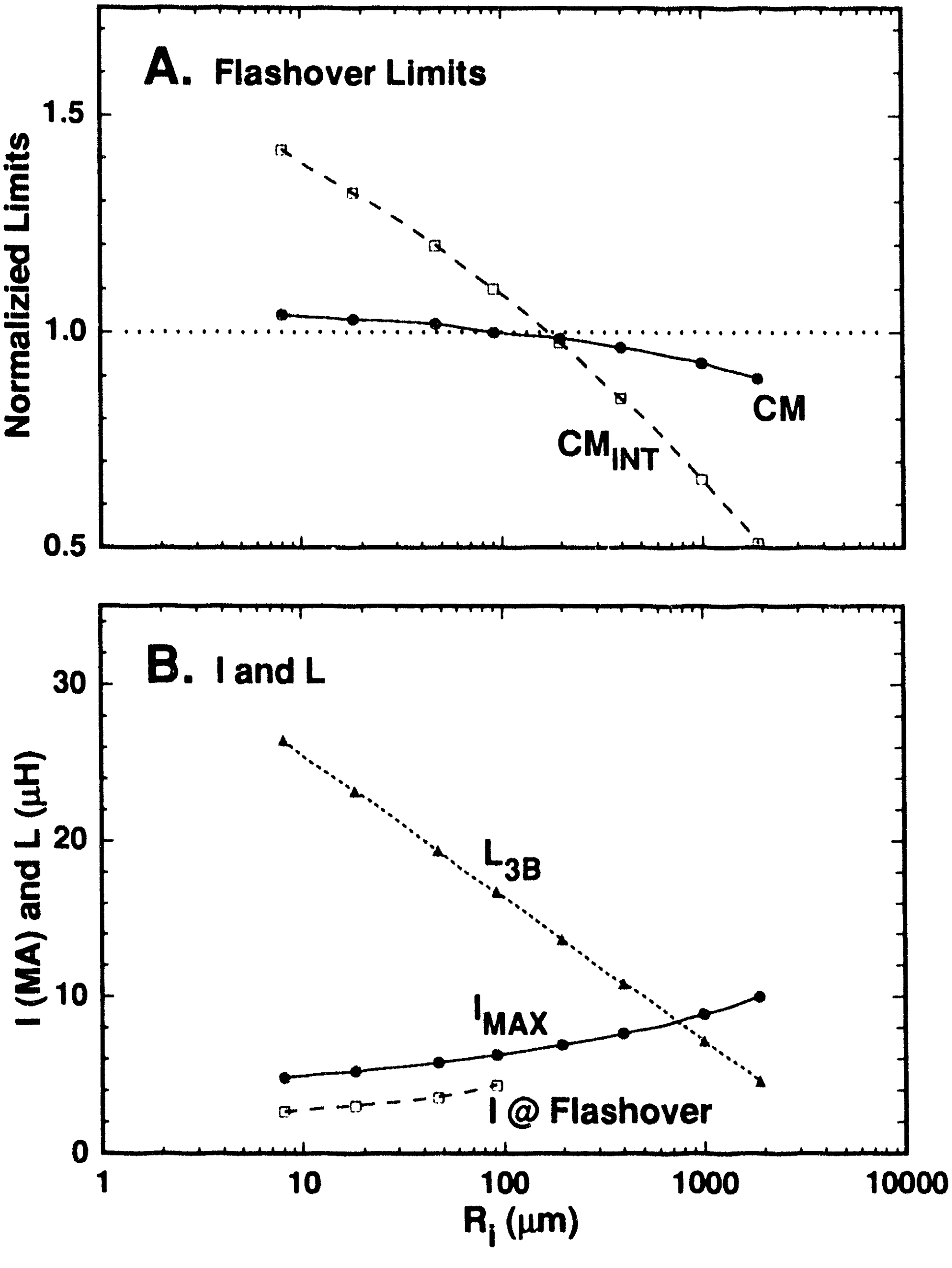

Figure 11. Comparison of (A) the electric field at the insulator stack normalized by the Charlie Martin limit (Eq. 6) [CM] and the Charlie Martin integral (Eq. 7) normalized by $175^6/A^{6/10}$ [CM_{int}] and (B) L_{3B}, the maximum current during implosions and that at insulator flashover as a function of initial radius of the array. Geometry and circuit corresponds to that of Figs. 1C and 2B, respectively, with $\ell = 2$ cm, $L_2 + L_{3A} = 8$ nH, and $R_0 = 6$ mm.

E. Dynamics versus Feed Inductance

Increasing the feed inductance by extending sizes in the feed region and that about the load, as illustrated in Fig. 12, reduces the current flow and increases voltages throughout the system, in analogy to reducing R_i as just discussed. Figure 13 compares the current calculated for the idealized geometry of Fig. 1C, which has a total vacuum inductance (i.e., $L_2 + L_3$) of 12.4 nH, with those of Fig. 12A and 12B, which have total vacuum inductances of 20.7 and 24 nH, respectively. In the next section we show that the use of the low-inductance idealized geometry of Fig. 1C, which generates the highest current in Fig. 13, is not practical because of electron losses in the feed near the load. On the other hand, use of the highest inductance geometry of Fig. 12, which has the highest potential for eliminating feed losses, just exceeds the CM flashover limit for masses in the range of interest. For example, the CM integral exceeds the flashover criterion (Eq. 7), 69 ns into the current pulse for a mass of 4.7 mg. So like the ~ 200 μm lower bound on wire diameter, ~24 nH represents an upper bound on the maximum feed inductance that can be tolerated for masses of interest.

On the positive side, however, the geometry of Fig. 12A has been shown experimentally to produce minimal electron losses in the feeds.[15] Its calculated characteristics as a function of mass are shown in Fig. 14, which should be compared with those calculated for the idealized geometry shown in Figs. 7 and 9. Comparison of Fig 14F with 7F illustrates how marginal the geometry of Fig. 12A is in enabling the fields to remain below the CM limit for masses of interest, namely those greater than a few mgs. Figures 13 and 14A show that for this 20.7-nH geometry, the maximum current achievable at implosion is about 5 MA. This optimum occurs for a mass of about 20 mg (Fig. 14A), 100 ns into the current pulse (Fig. 14B). For this mass, 150-kJ KE is transferred (Fig. 14C), which results in a velocity of 13 cm/μs at implosion (Fig. 14D). In contrast to this KE transfer optimum, the Mosher criterion (Eq. 1) is satisfied for a mass of 4.7 mg (Fig. 14E) similar to that calculated for the idealized geometry (Fig. 7E). In this case, the current flowing at implosion is 4.6 MA, with a maximum current of 5.4 MA flowing during the implosion process (Fig. 14A), which occurs about 20 ns before peak current for a high-mass load (Fig. 14B).

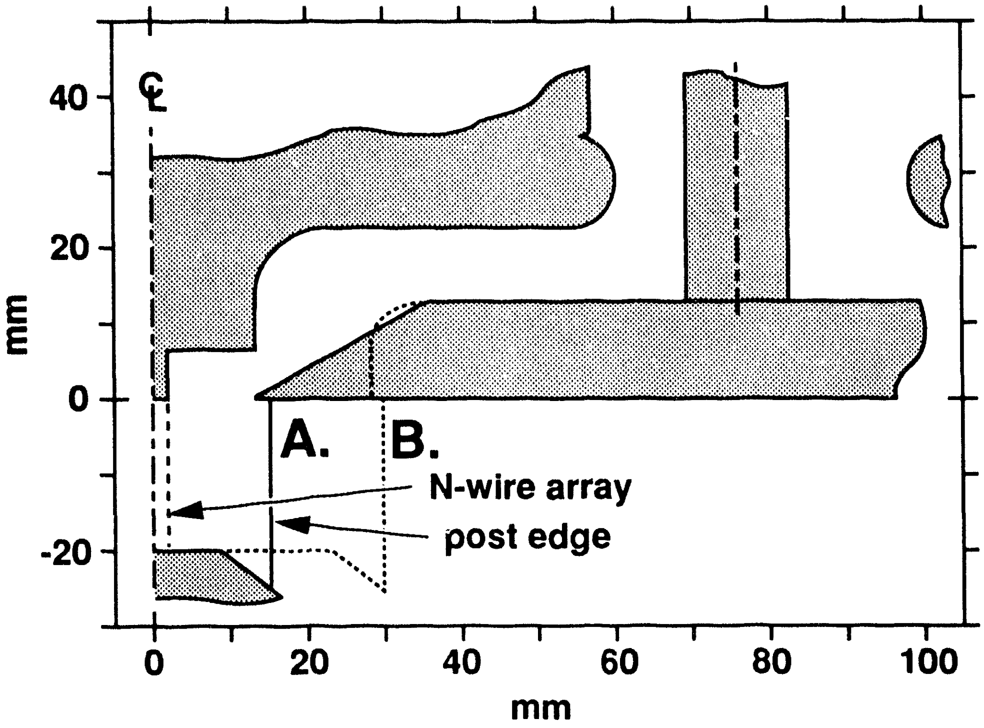

Figure 12. Realistic load and feed geometries corresponding to (A) $L_2 + L_3 = 20.7$ nH and (B) $L_2 + L_3 = 24$ nH.

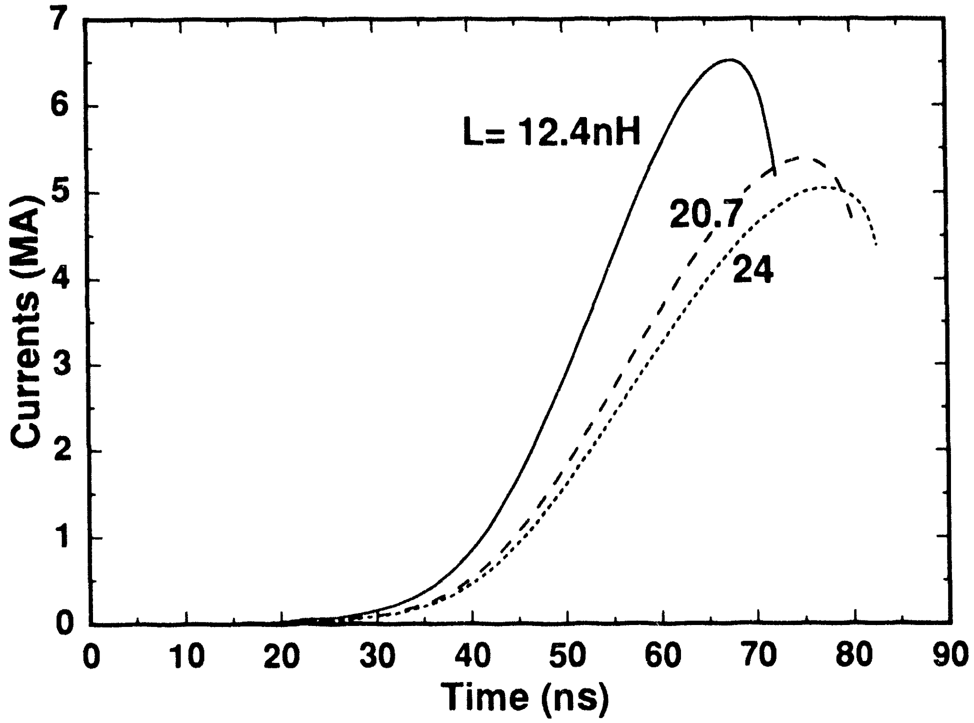

Figure 13. Comparison of current wave shapes corresponding to the geometry of (A) Fig. 1C with $L_2 + L_3 = 12.4$ nH, (B) Fig. 12A with $L_2 + L_3 = 20.7$ nH, and (C) Fig. 12B with $L_2 + L_3 = 24$ nH. m = 4.7 mg.

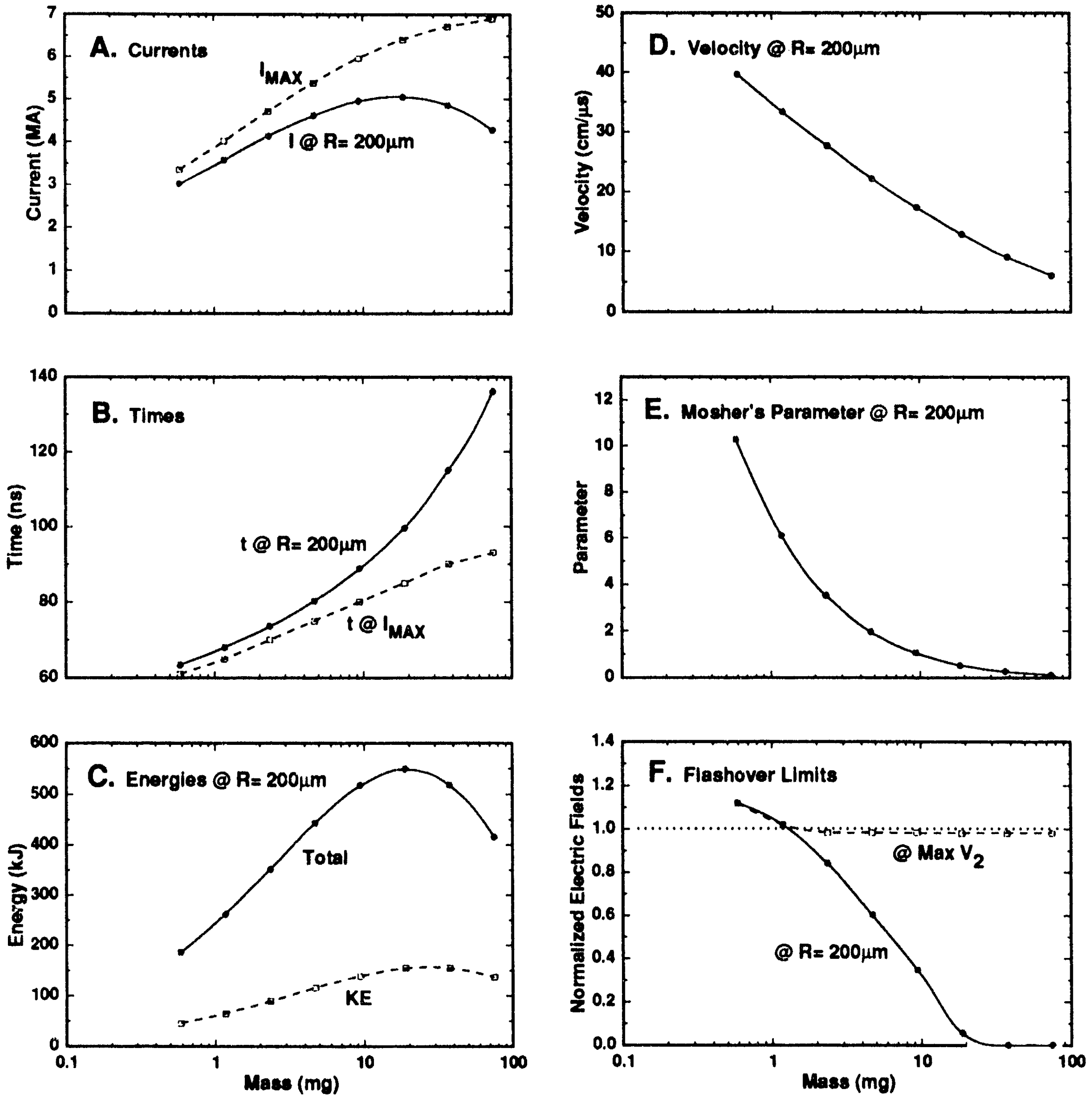

Figure 14. Comparison of (A) maximum current and current at implosion, (B) time of maximum current and implosion, (C) total system energy and KE transferred to the load at implosion, (D) velocity at implosion, (E) the Mosher parameter $[I/(m/\ell)]$ (see Eq. 1) at implosion, and (F) the electric field normalized by the CM limit (Eq. 6) at the insulator stack at the maximum voltage and at implosion as a function of load mass. Geometry corresponds to that of Fig. 12A and the circuit corresponds to that of Fig. 2B with $L_2 = 6$ nH, $R_i = 2$ mm, $R_0 = 15.7$ mm, and $\ell = 2$ cm.

III. Physical Characteristics of the Implosion

A. Overview

As we saw from Fig. 5, LASNEX and ZORK simulations agree with one another during the implosion phase. The difficult area to simulate lies in a region beyond the capability of ZORK, namely in the assembly and stagnation phases. For those phases, we have tried various versions of LASNEX, presently only in 1D. With plasma resistivities as calculated by LANL (15.0) and SNL (14.03) versions of LASNEX, the 1D simulations go to minimum radii roughly ten times smaller than observed experimentally,[16] with correspondingly higher electron temperatures than observed. Consequently, it appears that there are important features of the assembly and stagnation phases which these versions of LASNEX as yet do not properly simulate.

One of these missing features is likely related to the resistivity of the plasma. If the actual resistivity were significantly higher than calculated, magnetic flux (and current) would diffuse further into the plasma during the implosion phase and stop the implosion at larger radii (see Appendix C, Section VI, for example). In a simulated gas puff implosion, artificially increasing the resistivity tenfold gave a roughly correct minimum radius. However, the electron temperature did not decrease significantly as expected, suggesting there is more physics involved.

Another missing feature is the 3D nature of the load.[17] Rough analytic calculations indicate that the m = 0 (sausage/beading) and m = 1 (kinking/coiling) instabilities should develop significantly during the stagnation phase, causing dissipative processes to enhance the radiation output. 2D calculations are planned with the LLNL version of LASNEX, which has an improved resistivity model, and with the TIP code[18] (Appendix C, Section VI) to simulate the m = 0 instability.

With these caveats in mind the 1D-LASNEX wire array results for tungsten show the radius diminishing to tens of microns, the density reaching dozens of times normal tungsten density, and the plasma becoming very thick to the radiation. Due to the low outer temperature and the small emitting area, little radiation flux emerges from the wire during the stagnation. Simulated electron temperatures in the implosion core briefly exceed 1 keV but, even if such high values were real, they would not be observed through the surrounding optically thick tungsten.

As the radius decreases the magnetic fields and current densities rise to stupendous levels, comparable to those in a *neutron star.* The figures below show those values, along with the power dissipation and effective resistance as a function of radius at the time of minimum radius. (See also Ref. 14 for a discussion of the physical characteristics of the implosion from a single exploding wire.)

B. Initial Conditions and Radius-Time Plots

The following simulations deal with the two differing mass cases: (1) low mass, 4.7 mg, and (2) high mass, 37.4 mg. Figure 15 shows the modeled configuration. Because LASNEX, like ZORK, can only simulate cylindrical symmetry, the wires are represented by an equivalent mass cylinder. The calculations are begun with the cylinder already converted to a 1-eV plasma expanded to a thickness of 0.2 mm.

Figures 16A and 16B show the radius-versus-time plots of the low-mass (as in Fig. 5A) and high-mass cases, respectively. The outer zones (regions in the simulation) expand slightly due to the 1-eV initial temperature until the magnetic pressure overcomes it. For the low-mass case, the outer zone of tungsten reaches a minimum radius of 15 microns 73 ns after the start of applied voltage. The plasma bounces outward after the first pinch and recompresses at about 87 ns, but not to as small a radius (since entropy has been added to the plasma by shock waves during the first pinch). For the high-mass case, the outer tungsten zone reaches 59 microns at 101 ns. Observed minimum radii for gold wire arrays on Saturn are about 150 microns. Because the other pinch characteristics, such as temperature, density, etc., all depend strongly on the minimum radius achieved, the simulated imploded pinch characteristics are probably unrealistic. However, the simulated pinch characteristics at earlier times and larger radii may be more reasonable.

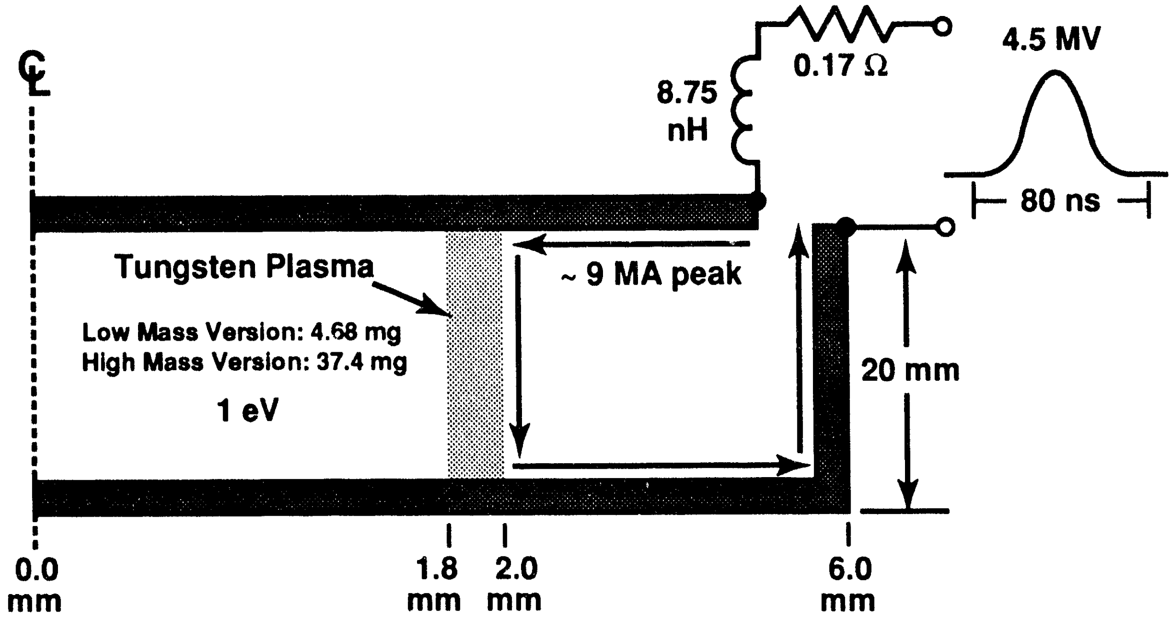

Figure 15. Physical configuration of LASNEX simulation.

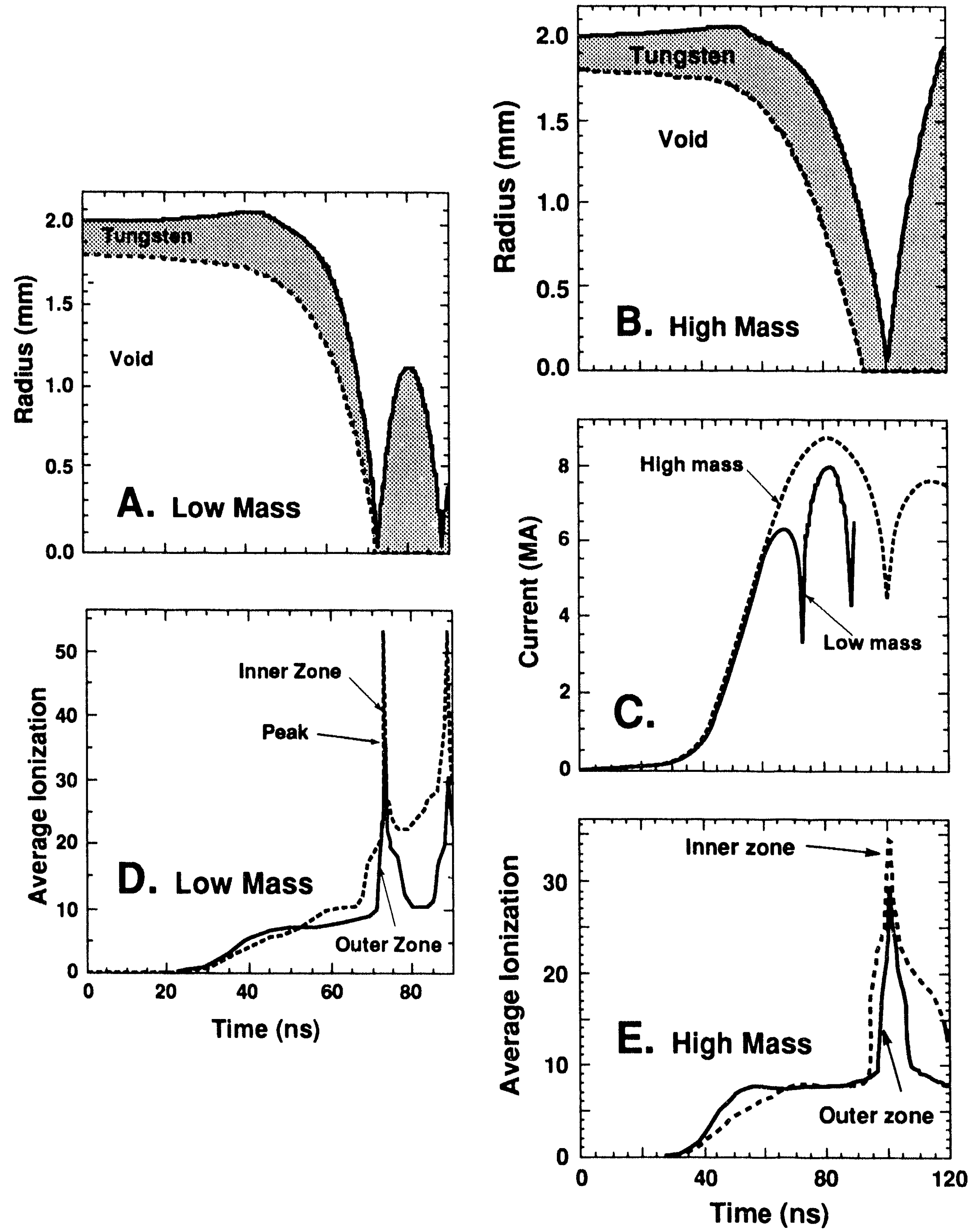

Figure 16. Radius of the inner and outer zones of the imploding tungsten cylinder as a function of time for (A) the low-mass case and (B) the high-mass case. (C) Current waveforms for both cases. (D) Average ionization in the inner and outer zones for the low-mass case. (E) Average ionization in the inner and outer zones for the high-mass case.

C. Currents, Velocities, and Ionizations

Figure 16C shows the current waveform for each case. Since the first pinch of the low-mass case occurs 22 ns before the time of maximum short-circuit current (about 95 ns), it utilizes less of the available machine energy than the high-mass pinch. The low mass achieves a higher outer zone velocity (30.9 cm/μs, compared to only 13.3 cm/μs), yielding a 5.4 times higher kinetic energy per ion (~ 92 keV).

Kinetic energy per ion should be a major factor in determining the degree of ionization of the plasma during the pinch. Figure 16D(E) shows the average ionization evolution at the innermost and outermost zones of the low(high)-mass case. For both, the tungsten ($Z = 74$) load easily loses 8 of its electrons to become Dysprosium-like. The next slight plateau in the ionization curve of Fig. 16E occurs at an ionization of 20, representing a broad range of M-shell states where Ni-like is very stable. For the low-mass case, the average ionization reaches a peak of about 53 (nearly calcium-like ions), while the high-mass case only reaches 35 (nearly strontium-like ions). In real pinches, the ionizations should be smaller.

D. Temperatures and Opacities

Figure 17A compares the radiation temperature profiles at the time of minimum radius for each case. A rough rule of thumb is that each 20% decrease of radiation temperature represents one radiation mean free path, so the large variations in radiation temperature shown implies that in both cases the tungsten has become more than several mean free paths thick to its own radiation. This profile suggests that the simulations proceeded in the classical radiation collapse mode (radiation loss exceeding ohmic heating) until the plasma reached high opacities. At that point the plasma could no longer radiate energy efficiently, causing the internal temperatures to rise until the pressures balanced out the applied magnetic forces. In other words, a hypothesis is that the opacity stopped the pinch in the simulations. Further examination of the outputs may be able to confirm or deny this hypothesis.

Figure 17B(C) shows the inner-zone and outer-zone radiation temperatures versus time for the low(high)-mass case. Because the opacities are high at implosion, the electron, ion, and radiation temperatures in the interior are nearly identical, although the simulation conditions (3-temperature, non-LTE) would have permitted them to be different. In the outermost zone of the low-mass case, the ion temperature exceeds the radiation temperature by about 35% at the time of minimum radius, but at other times the two are within a few percent of one another. The electron temperatures are always within a few percent of the radiation temperatures. All these temperatures near the time of minimum radius are unrealistically high.

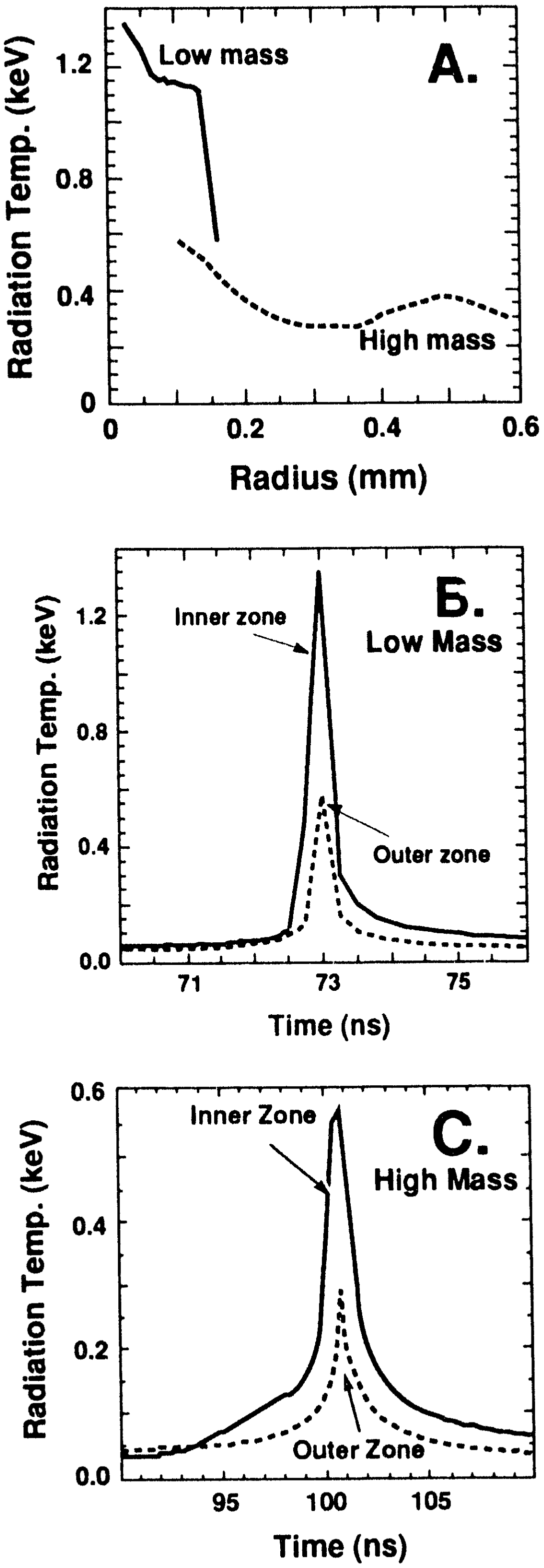

Figure 17. (A) Radiation temperature profiles at the time of minimum radius for each case. (B) Inner- and outer-zone radiation temperatures versus time for the low-mass case. (C) Inner- and outer-zone radiation temperatures for the high-mass case.

E. Radiation Outputs

The low-mass simulated radiation output peaked at 21 TW; for the high-mass case the peak was 4.2 TW. The radiation pulses were very short. Table I compares the total radiation outputs in kilojoules above 1 eV, 1 keV, and 10 keV for the two cases.

Table I
Simulated Radiation Outputs in kJ

	Low Mass	High Mass
> 1 eV	58	29
> 1 keV	12	1.6
> 10 keV	0.1	4×10^{-9}

These radiation outputs are less than 20% of those for a typical gas puff z pinch on Saturn. The main reasons are that (1) at the time of minimum radius only the surface can radiate, (2) the temperature of the surface is rather low, and (3) the area of the surface is relatively small.

Figure 18 shows the radiation spectra at the times of peak output for each case. A peak possibly due to *M*-lines (~ 1-2 keV) appears in each spectrum. The low-mass spectrum shows considerably more output above 1 keV than does the high-mass spectrum. Also, the low-mass spectrum shows a peak possibly due to *L*-lines (~ 7-12 keV); there is almost no sign of such a peak in the high-mass spectrum. The difference between these spectra is due to the large difference in electron temperatures and ionizations caused by the large difference in implosion velocities. These spectra show that *purely thermal* radiation from high-z wire arrays is not at all likely to produce the high energy component we want.

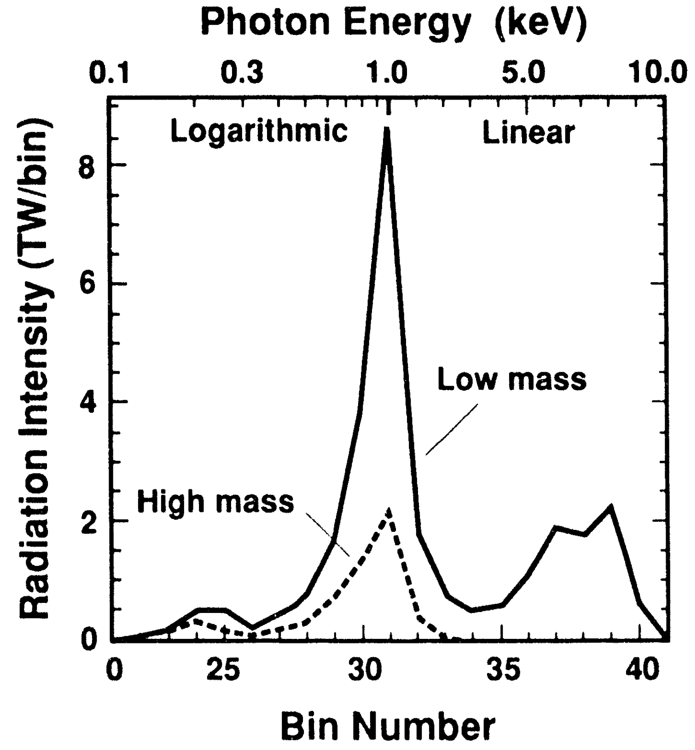

Figure 18. Radiation spectra at the times of peak output for each case.

F. Electromagnetic Quantities

Figure 19A shows the radial profile of B_θ (the other components are zero in the simulation) in the low-mass case at the time of minimum radius. Because the radius of the pinch is very small in the simulation, the field exceeds 600 MG, an unrealistically high value. Assuming negligible displacement current, Maxwell's equations relate the current density J to the radial profile of B_θ:

$$J = \frac{1}{\mu_0 r} \frac{\partial}{\partial r}(r \ B_\theta)$$

Using this equation on LASNEX's output of $r\,B$ gives the current density profile in Figure 19B. Figure 19C shows the profile of the calculated electrical conductivity, σ, at the same instant. Since the plasma has stagnated, the velocity is very low and $\mathbf{v} \times \mathbf{B}$ can be neglected. Ohm's law then provides the electric field E

$$E \approx \frac{J}{\sigma}$$

shown in Figure 19D. The reversed field in the outer layer of plasma may be due to $\mathbf{v}\mathrm{x}\mathbf{B}$ terms from the expansion. The total power dissipation P is:

$$P = 2 \ \pi \ \ell \int_0^a \frac{J^2}{\sigma} r \ dr,$$

where ℓ is the length of the pinch, and a is its radius. For the low-mass case, P was 42 TW at the time of minimum radius. The effective resistance R of the pinch is:

$$R = \frac{P}{I^2}$$

where I is the total current at that instant. The resulting resistance was 3.78 ohms.

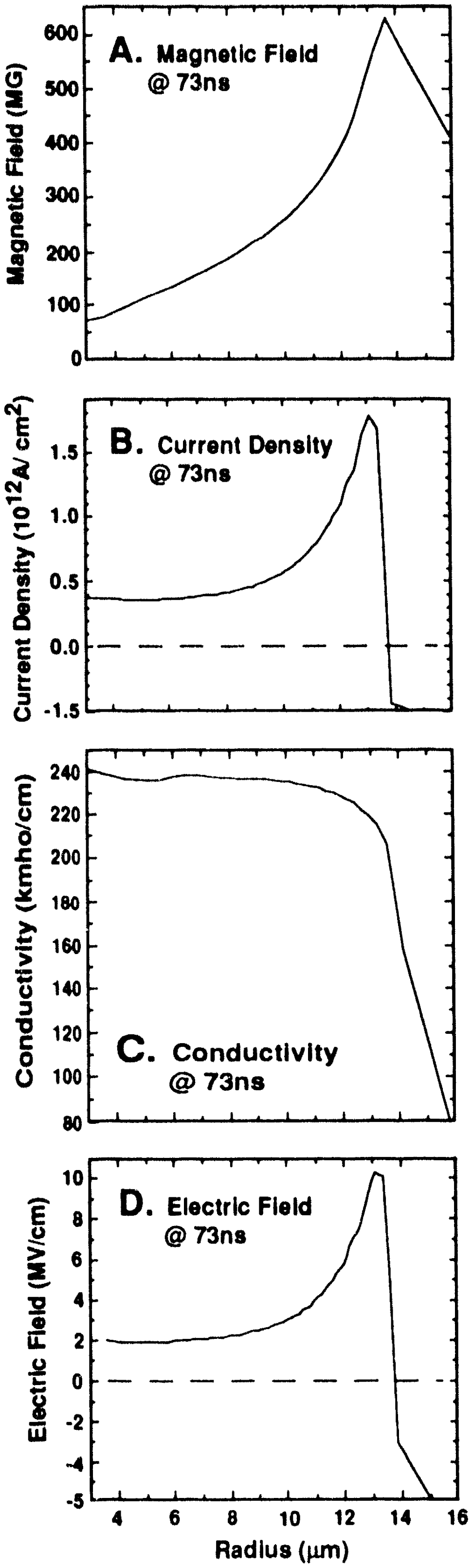

Figure 19. At implosion for the low-mass case (A) magnetic field, (B) current density, (C) conductivity, and (D) electric field as a function of radius.

IV. Electron Loss Near Load

A. Overview

Excessive electron loss in the feed can lead to the formation of a plasma on the anode and to subsequent arcing with decreased current through the wire load. In this section, we examine the likelihood for this scenario for the three geometries of Fig. 1C, Fig. 12A, and Fig. 12B using the TWOQUICK code to simulate the electron flow in the feed region and the CYLTRAN code to estimate the subsequent energy deposition in the anode from the loss electrons.

B. TWOQUICK Simulations

The electromagnetic PIC code MAGIC[19] has been replaced for much of our simulation work by the code TWOQUICK. This code contains the same physical models with some improvements in numerics and diagnostics, and much more flexibility in post-processing of the output data, an important feature in the large and expensive simulations typically performed over the past few years for PBFA, SABRE, Jupiter, etc. To aid in understanding the Saturn experiments, a TWOQUICK model was developed specifically for the study of electron losses near the load as a function of geometry and time.

The first setup modeled is shown in Fig. 20A, based on the geometry shown in Fig. 1C, with the voltage input derived from the ZORK circuit of Fig. 2B. Several models for voltage application were examined. The most general model at the input (R = 5.7 cm in Fig. 20A) is to attach a transmission line model which calculates the voltage V and current I in the Saturn feeds and insulator (Figs. 1A and 1B). This calculation was done with a model including line impedances of 0.17 Ω, 0.083 Ω, 1 Ω, and 20 Ω (to match to the radial disk feed in Fig. 20A). The corresponding transit times in these regions are 135 ns, 9 ns, 3 ns, and < 1 ns. Because small cells (sub-mm) must be used to resolve the PIC region of Fig. 20A, this means wasting on the order of 10^5 PIC time steps before the pulse reaches the region of possible electron loss near the load. Thus it was decided to simply apply V_2 or V_3 from the circuit calculations directly to the input.

The other big issue in constructing this model is how to represent the load. Obviously the detailed load physics cannot be included in our PIC simulation, and it is unnecessary anyway since our goal is to calculate electron loss in the regions feeding the load. In fact, the simplest load model would be a short circuit (perfect conductor in TWOQUICK), and this was found to work fairly well until late in the pulse. However, losses during implosion are of interest here, so after some trial and error we settled on using a model wherein the load voltage V_4 (from ZORK with $m = 4.7$ mg and $\ell = 2$ cm) is applied to the problem at R = 2 mm. This in turn determines tangential E at this boundary and is a sufficient boundary condition to yield a solution.

Next we describe the main results of the TWOQUICK modeling. For idealized geometries such as that in Fig. 20A, the electron losses are concentrated near (within a few mm) the anode corner and are large enough to lead to plasma formation and arcing. As the input voltage builds in the TWOQUICK simulation (Fig. 20B), the currents in the feed (Fig. 20C) and in the load (Fig. 20D) increase to above 5 MA. Most of this current flows in the boundaries. The emitting cathode, however, also yields electrons that clump into vortices (as often seen in MITLs) which cross too near the anode, allowing electron "scrape-off" at the corner (Fig. 20A). These losses to the anode as a function of time are summarized in Table II:

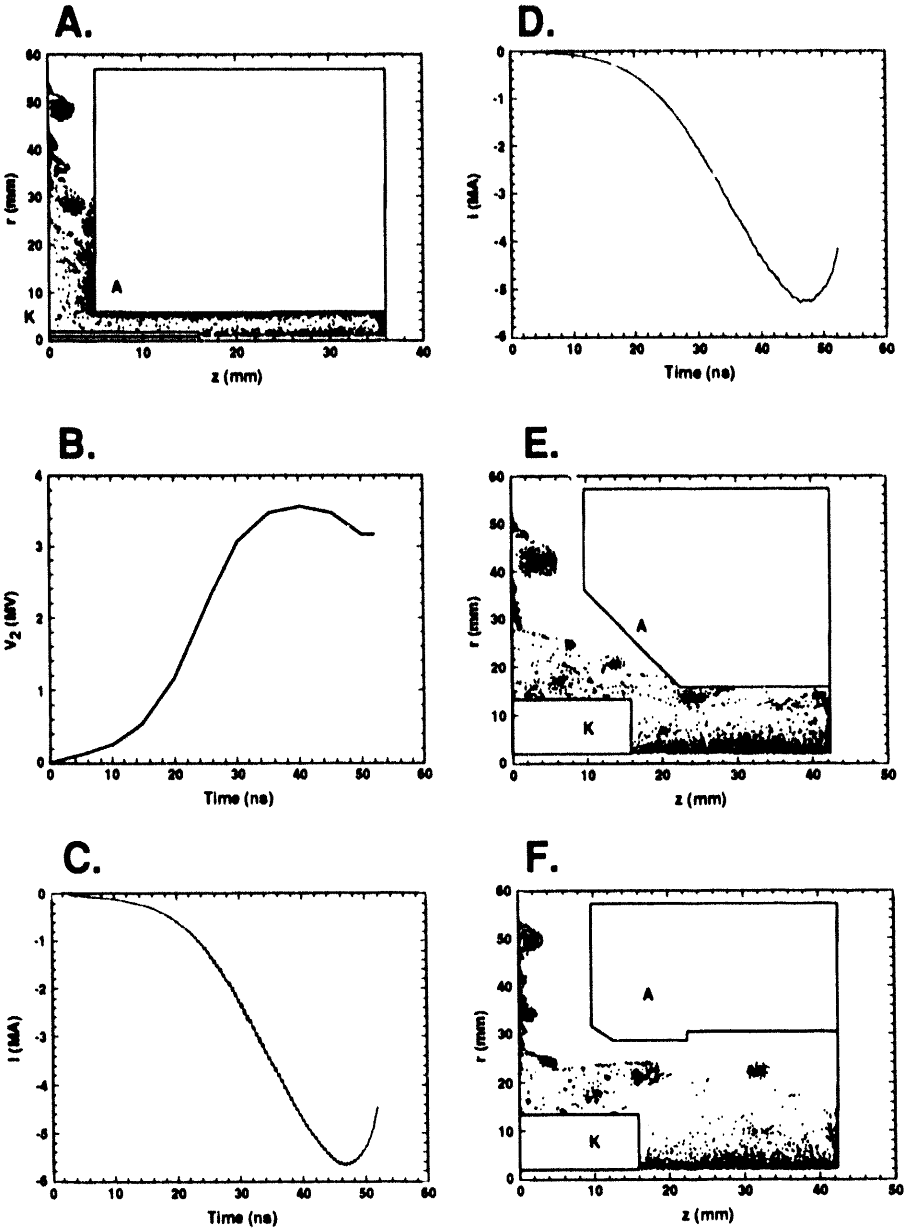

Figure 20. (A) Electron map at 48 ns for Setup #1, as modeled by TWOQUICK. The cathode, anode, and load regions are denoted by K, A, and L. This PIC calculation only calculates the Saturn system of Fig. 1C inside radius R < 6 cm. Note the pile-up of electrons near the inner anode corner, where the only significant loss occurs, 81 kA at t = 48 ns. The applied voltages are V_2 at R = 5.7 cm and V_4 (load voltage) at R = 2 mm, as determined from ZORK runs. (B) Input voltage V_2 for Fig. 20A, Setup #1. (C) Input current for Fig. 20A, Setup #1. (D) Load current for Fig. 20A, Setup #1. (E) Electron map at 45 ns for Setup #2. The larger feed gap and sawed-off anode corner lead to negligible loss. Input voltages: V_3 and V_4 from ZORK. Max load I = 5 MA. (F) Electron map at 50 ns for Setup #3. The electron loss to the anode, although larger than in Setup #2, is much less than in Setup #1 and should not cause plasma formation problems. The orientation of the geometry shown in (A), (E), and (F) is that of Fig. 1C inverted and rotated by 90°.

Table II
Electron Losses to Anode in Fig. 20A

Time (ns)	9.6	19.2	28.8	38.4	48.0	51.2
I (kA)	5	6	26	111	151	104
ε (MeV)	0.3	0.4	0.7	0.6	1.0	1.5

where the times correspond to the pulse shown in Figs. 20B-20D and ε corresponds to the KE of the lost electrons. While a 100-kA loss is a small part of the total current (5 MA), it is of concern for arcing. Thus we turn to another setup.

Setup #2 is shown in Fig. 20E and is identical to that of Fig. 12A, which has been shown experimentally[16] to provide relatively lossless power flow to the load. Here we have chopped off the anode corner and increased gap dimensions (at the cost of larger inductance). Although some electrons still exhibit **ExB** drift near the lower anode corner, *the loss is now negligible*. The input voltages here are V_3 (@ R = 5.7 cm) and V_4 (@ R = 2 mm) as calculated by ZORK. The resulting load current of about 5 MA does not differ substantially from Fig. 20D. Details of the electron flow were checked every 5 ns to the time of implosion.

A compromise Setup #3, with some anode corner reduction, is shown in Fig. 20F. It is identical to that of Fig. 12B. Again we apply ZORK voltages V_3 and V_4. The loss to the anode is small and peaks early in time (< 1 kA at 10 ns). Again, the V's and I's were approximately as before, and the electron flow was plotted every 5 ns. The simulation indicates that no plasma formation should occur due to electron deposition.

In summary, we have made a TWOQUICK model based on circuit code input to study electron flow near the load in Saturn. For small-gap sharp-corner setups, the electron loss is large enough to cause problems with anode plasma formation; this is studied with CYLTRAN (next section). However, it appears to be easy to find setups with small or negligible anode loss by simply changing the anode shape as shown in Setup #2.

C. CYLTRAN Simulation

The TWOQUICK model yields the coupled space-angle-time distributions of the electron loss current at the anode surfaces. We are concerned here with the possibility that energy deposition from this loss current may be sufficient to initiate formation of an anode plasma that would cause premature impedance collapse. We describe here the simulation of this energy deposition by a Monte Carlo code which employs the output of a TWOQUICK simulation as its input, for the geometry of Setup #1 (Fig. 20A).

The coaxial solid-annulus anode is exposed to loss currents along its inner cylindrical surface and its upstream planar boundary. The TWOQUICK model predicts that the current density reaches a maximum at the inner radius of the planar surface. With the spatial resolution employed by the model, this planar annular region is bounded by the inner radius of the anode (6.0 mm) and a radius of 7.6 mm (Fig. 20A). The peak loss current in this region reaches about 80 kA, 48 ns into the pulse (Table II). The 1.0-MeV kinetic energy of the electrons at this time is also near the maximum for this region.

We decided to calculate the energy deposition in this critical region as the most likely location for the formation of an anode plasma.

The surface of the anode is resolved into a number of regions for scoring the loss current distributions. For each surface region of the anode and for each time interval (usually 4.8 ns), TWOQUICK yields the KE of the electrons, the loss current, the mean polar angle of incidence (azimuthal velocity component is zero) of the electrons, and the width (sigma) of an assumed Gaussian distribution of the incident angles. It is from this information that the source distribution for the Monte Carlo simulations is obtained.

The energy deposition in the anode was simulated using a modified version of the CYLTRAN Monte Carlo code. CYLTRAN is the two-dimensional axisymmetric code from the ITS (Integrated TIGER Series) system of coupled electron-photon radiation transport codes.[8,9] The system employs a sophisticated physical model for simulating the production and transport of the electron-photon cascade from 1 GeV down to 1 keV with or without macroscopic electric and magnetic fields. The R-Z geometry of the CYLTRAN code is especially suited to beam geometries.

Because the ITS codes are time independent, a separate calculation was performed for the critical region ($6 < R < 7.6$ mm) at each output time of the TWOQUICK code simulation for which there was significant loss current (Table II). The energy deposition was obtained by weighting the predicted deposition rate by the appropriate time interval. Each calculation was for the monoenergetic source predicted by the TWOQUICK code. The current predicted by TWOQUICK was assumed to be distributed uniformly over the critical region. Thus, the space and energy dependence were accounted for with minor modifications to the Monte Carlo code.

The polar angle of incidence was sampled from a Gaussian distribution using the algorithm of Kahn[20] with two rejection conditions. First, the sampled angle was rejected if it was more than three sigma from the mean. Thus, only about 0.2-0.3% of the sampled angles were rejected for this reason. More likely were those samples that were rejected for being greater than 90°. Because the mean angles ranged from 44° to 57° and the widths ranged from 19° to 41°, rejections under this criterion were more frequent. Still, the number rejected was usually well below 10%. When rejection occurred, the polar angle was simply resampled until an acceptable value was obtained.

The most significant modification of the CYLTRAN code was the incorporation of specular reflection. Because of the relatively high angles of incidence, there is a significant probability for collisional reflection from the stainless anode and even for escape from the inner cylindrical surface of the anode. There is a high probability that these escaping electrons would be reinjected by the self-consistent fields of the diode. If these fields could be specified, their effects could be simulated by the ITS codes, but their accurate specification is not yet practicable. Instead, their effects (e.g., reinjection) are simulated in the present analysis by localized specular reflection at the point of escape.

Results of the Monte Carlo simulations are summarized in Table III. Deposition is given for the subzone of maximum energy deposition and corresponds to the innermost radial increment of the anode and the most upstream axial increment. The statistical uncertainties of the tabulated energy depositions are 2-3%, resulting in negligible uncertainty in the total deposition. A small amount of deposition at earlier and later times than those shown in Table III are unaccounted for. The strong axial focusing observed in Fig. 20A suggests the uniform current density assumption should underestimate the deposition. On the other hand, the localized specular reflection assumption does not accurately simulate the probable radial diffusion along the surface. This diffusion must mitigate the radial focusing to some extent.

Table III
Source Parameters for Critical Region

Last column is the calculated average deposition in the first 0.005 mm of depth for a radius between 6.0 and 6.4 mm in units of Joules/gram per Coulomb deposited.

time (ns)	Kinetic energy (MeV)	Loss current (kA)	θ (°)	$\delta\theta$ (°)	Δt (ns)	Energy Deposition (J/g-C)
19.2	0.36	4.2	57	41	4.8	1.01×10^7
24.0	0.58	6.5	47	31	4.8	1.06×10^7
28.8	0.69	16.5	45	29	4.8	1.09×10^7
33.6	0.89	35.4	45	25	4.8	1.07×10^7
38.4	0.62	60.0	44	22	4.8	1.05×10^7
43.2	1.10	70.6	44	19	4.8	1.11×10^7
48.0	1.00	79.8	46	22	4.0	1.11×10^7
51.2	0.81	55.0	44	24	4.8	1.03×10^7

Summing the products of the energy deposition (last column of Table III) times the loss current (third column of Table III) times the interval Δt (difference in time between the sequential times of Column I of Table III) for each time (totaling 1.5 mC of loss charge) predicts an total deposition of 16 kJ/g in the subzone of maximum energy deposition. This value far exceeds the 200 to 300 J/g necessary to initiate an anode plasma.[21] The value, in fact, is well beyond the 8.7 kJ/g required to vaporize the anode surface.[22] Thus, the idealized low-inductance configuration of Fig. 1C and Setup #1 is likely not suitable for delivering power to the load and one is limited to higher inductance configurations as shown in Fig. 12.

V. Summary

The TWOQUICK/CYLTRAN simulations give credibility to the experimental observation that load geometries like that of Fig. 12A provide relatively loss-free power flow in the region of the load. Using such geometries in ZORK, calculations of compact 2-cm long wire arrays having masses of 4 to 5 mg show that the empirical Mosher criterion (Eq. 1) for the maximum production of non-thermal radiation can be satisfied. For such arrays with initial radii of 2 mm, peak currents of ~ 5 MA can be driven through the arrays with implosions occurring ~ 20 ns before the driving voltage reverses. This delay is potentially sufficient for the $m = 0$ instability and subsequent non-thermal radiation to occur via the Mosher mechanism. Moreover, the analyses indicate that for masses greater than 1 mg, electric fields at the insulator stack remain below the CM flashover limit, so the full current developed should flow through the load. Accordingly, an experiment using such configurations is underway to verify the Mosher expectations at the 5-MA level.

The ZORK calculations also show that the maximum energy transfer to the load occurs for masses in the 20- to 40-mg range and can be as large a 150 kJ out of a total system energy of 550 kJ at implosion for 2-cm long arrays. The calculations show that, for arrays having radii less than ~ 200 μm or geometries with vacuum feed inductances greater than ~ 24 nH, the electric field at the insulator stack exceeds the CM limits during the power pulse, limiting the potential current flow to the load. Thus, for full performance implosions, the calculations suggest that radii and inductances should remain above and below these values, respectively.

Although the 1D LASNEX calculations with tungsten show excessive compression to very small radii with correspondingly unphysical results at the minimum implosion radius, they do give credibility to the calculations of the revised ZORK code. Moreover, they provide an estimate of the physical characteristics of the tungsten during the implosion process. Future theoretical work will build on these result using the recently released 2D LASNEX code and the new TIP code (Appendix III)[18] to evaluate the conditions necessary to initiate the m = 0 instability—the precursor necessary for the non-thermal radiation production via the Mosher bremsstrahlung mechanism. Additionally, when these results are combined with the IPROP[23] code for modeling the subsequent non-thermal electrons and associated bremsstrahlung, the potential exists for theoretically verifying the Mosher mechanism and comparing with the results of the 5-MA experiment.

VI. Appendices

A. Calculation of Currents in a Saturn Center-Wire-with-Posts Load

To verify on Saturn Mosher's earlier work with single axial wires on Gamble II, it was suggested that a single on-axis wire could be surrounded by a set of non-radiating posts that would divert current from the center wire to reduce the load inductance and avoid insulator flashover (Fig. 21). To be useful, 10% or more of the machine current must pass through the wire load. A numerical calculation was done to determine the initial current division between the posts and wire in this system.

The calculation was performed assuming that the posts and wire are perfect conductors (or initial resistance low compared with inductive reactance). The posts and center wire are connected together at the top and bottom by zero resistance plates. Then

$$\oint_L \mathbf{E}\cdot ds = \frac{\partial}{\partial t}\oint_A \mathbf{B}\cdot n dA = \frac{\partial \Phi}{\partial t} = 0$$

where **E** is the electric field along a closed path L inside the conductor, where E is zero, and Φ is the net flux passing through the area A enclosed by the path (Fig. 22). Since this flux is zero at t = 0, and its time rate of change is zero, it is always zero. The flux is that produced by all currents in the system. The loop was chosen to take advantage of the array symmetry, so the field is normal to the plane of the loop everywhere in the loop.

This flux was calculated, and the current division between the wire and all posts was iterated in the code to drive the flux to zero, producing the desired current division. Fields of filamentary currents were used, with flux inside the wire and post radii set to zero. Any effects of image currents or non-uniform current distributions in finite-size conductors were ignored. The flux was calculated using a MATLAB-based[24] routine developed for analysis of highly uniform magnetic fields for magnetic resonance imaging applications.

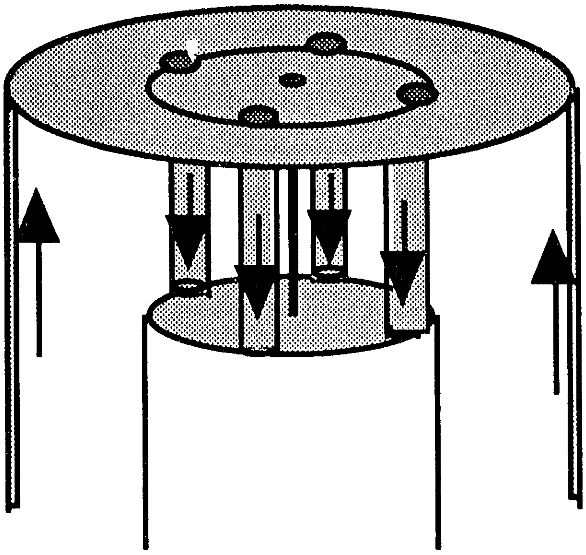

Figure 21. Saturn wire-and-post load showing directions of currents in the outer cylinder and posts. Center wire current is in the same direction as in the posts.

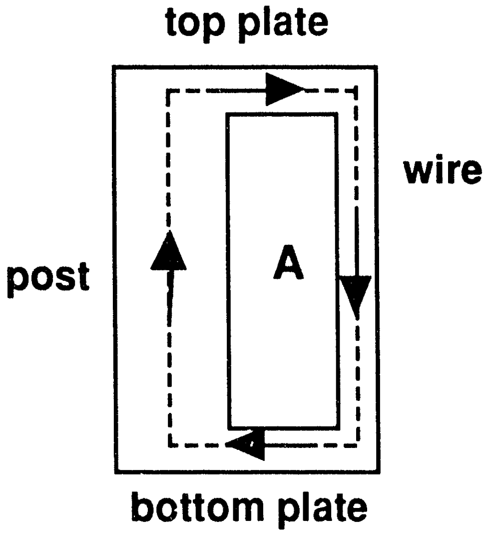

Figure 22. Schematic of path L in post and wire surrounding area A.

Results are shown in Figs. 23 and 24. Fig. 23 shows center wire current as a function of wire diameter for four posts of 0.5-, 1-, and 2-mm diameters. Fig. 24 shows the effect of changing the number of posts, using 0.025-mm (1 mil) diameter wires and 1-mm diameter posts. The ratio of radius of the post circle to that of the outer current return cylinder (or the distance between the center wire and the radius of the post circle) had relatively little effect on the current division between the posts and center wire.

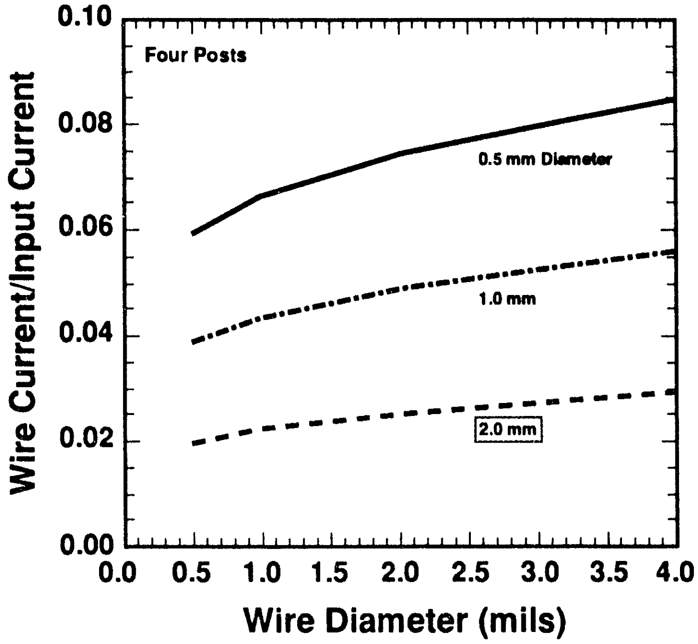

Figure 23. Wire current vs. wire diameter.

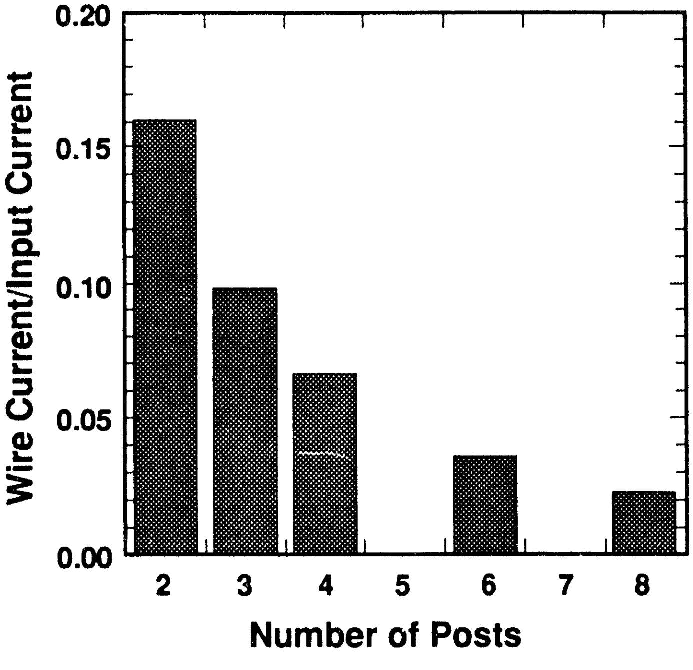

Figure 24. Wire current vs. number of posts with 0.5-mm diameter posts and 25-μm wire.

It appears from these calculations that there may not be a practical configuration that will produce 1 MA or more of the 8-10 MA available in a Saturn wire-and-posts load. The two-post case does have more than 10% of the load current in the center wire, but this configuration would have to be examined to evaluate the effects and risks of asymmetries of the current.

B. Calculation of the Inductance of Saturn Wire Loads

1. General Considerations

Inductance calculations were done for Saturn loads of several fine wires located on a circle, surrounded by return current posts on a larger radius circle. It is usually convenient to approximate the inductance of this configuration by assuming the outer post ring and inner wire circles are continuous cylinders, and doing an analytic calculation. The following calculations indicate the accuracy of that approximation is within 10% to 25%, and that the inductance is higher than the cylindrical approximation. Comparisons are made between the cylinder and post cases in examples listed below.

The inductance of the system of posts and wires (or cylinders and wires) was derived numerically by calculating the magnetic energy per unit length in an infinitely long array of filamentary currents and multiplying by the actual array length. Calculations were also done for the load wire arrays with a continuous cylinder in place of the posts. Comparison also is made with the low-frequency (flux allowed inside the conductors) analytic formulas found in F. W. Grover, *Inductance Calculations*.[25]

The formula in Grover, Chapter 5, for the inductance of a set of round conductors on a circle inside a cylinder is

$$L(\mathrm{nH/m}) = 200\left[\log\frac{r}{a} + \frac{1}{n}\log\frac{a}{n\rho} + \frac{1}{4n}\right],$$

where ρ is the cylinder radius, a is the wire circle radius, r is the wire radius, and n the number of wires. Three terms have been omitted in transcribing this from Grover, one of which is zero and two of which cancel when the thickness of the cylinder becomes zero (no flux in the cylinder wall). In this formula, uniform current distribution is assumed in interior of the wires.

The magnetic field of the arrays was numerically calculated using a MATLAB-based routine developed for analysis of highly uniform magnetic fields for magnetic-resonance imaging applications. In a system of infinite-length wires, the magnetic field of each wire is

$$\mathbf{B} = \frac{\mu_0 I}{2\pi r}\hat{\varphi},$$

so the total field is simply the vector sum of fields of the individual wires. The calculation is accurate to the extent that the currents can be represented by filaments. Not included (except for estimates described below) are effects of conical wire-support ends or image currents in the finite size posts. The mesh field was set to zero in cells near the wires and an analytic formula used for the field energy in that region. A wire diameter of 0.005 cm (2 mils) and array length of 2 cm was assumed.

Calculations of fields in configurations with return currents in a continuous cylinder were done using the method of images. Magnetic current images follow exactly the derivation of electric images found in most electromagnetics textbooks. The requirement div**B**= 0 implies that the component of **B** normal to the cylinder surface must be zero (**B** in the conductor is zero), that is, **B** is entirely in the ø direction at the cylinder surface (Fig. 25). All currents in this system are in the z direction, and **A** is parallel to the currents, so **A** has only z-components. Then

$$\mathbf{B} = \nabla \times \mathbf{A} = \frac{\partial A_z}{\partial \varphi}\hat{\mathbf{r}} + r\frac{\partial A_z}{\partial r}\hat{\varphi},$$

and

$$B_r = 0 = \frac{\partial A_z}{\partial \varphi}$$

so A_z is constant (analogous to the electric potential V) on the cylinder surface. This boundary condition may be satisfied by an image current such that

$$I_{image} = -I_{real}, \text{ and } r_{image} = R^2/r_{real},$$

as shown in Fig. 25.

The accuracy of the calculation is, of course, not good to the three digits quoted here, but the primary conclusion is that the coaxial cylinder approximation (with the outer cylinder radius equal to the radius of the circle through the centers of the posts) for an array of 12 or more wires and 8 large diameter return current posts in these configurations underestimates the inductance by 10% to 25%, as in the examples below. The conical top, not included in this calculation, may add about 10% to the actual inductance.

2. Effects of Changing Wire Diameter

The inductance is relatively insensitive to the wire diameter for these small wires. Reducing the wire diameter by a factor of 2 typically increased the calculated inductance by less than 5% in either the numerical or analytic calculation for a 12-wire array, and less than 3% for a 24-wire array in the examples listed below.

3. Current Distribution in the Posts

The effects of current distribution on the surface of the large posts could be included in this filamentary current calculation by iteratively calculating image currents in the posts. However, an estimate of a reasonable worst-case (largest posts) effect on the current distribution in the posts can be made graphically, and using this in the MATLAB inductance calculation indicates that the effect will be to decrease the inductance by a small amount. The calculation of image currents in conducting cylinders is the inverse of the image current calculation described above, requiring the interchange of the labels real and image, with the addition of an image current at the cylinder center with the sign of the current opposite that of the image.

Because it is necessary to have open lines-of-sight between the posts, the largest post radius usable is approximately one-fourth the post circle radius in an eight-post system (Fig. 26). For a first-order estimate, consider the currents in each post to be located at the post center, and the currents in the load wires to be a single (total) current located at the system center. Manually drawing the locations of the images in a given post of the above radius, a close approximation of the net effect of the images is to move the filamentary post current from the post center radially inward to a point one-fourth the post radius nearer the system center. Keeping the posts in the same location (that is, the flux exclusion regions of the posts stay at the original radius) and moving all post current locations the indicated R/4, decreased the calculated inductance by less than 1%. Even if the effect is a factor of five larger, it is small compared with end and finite-length effects.

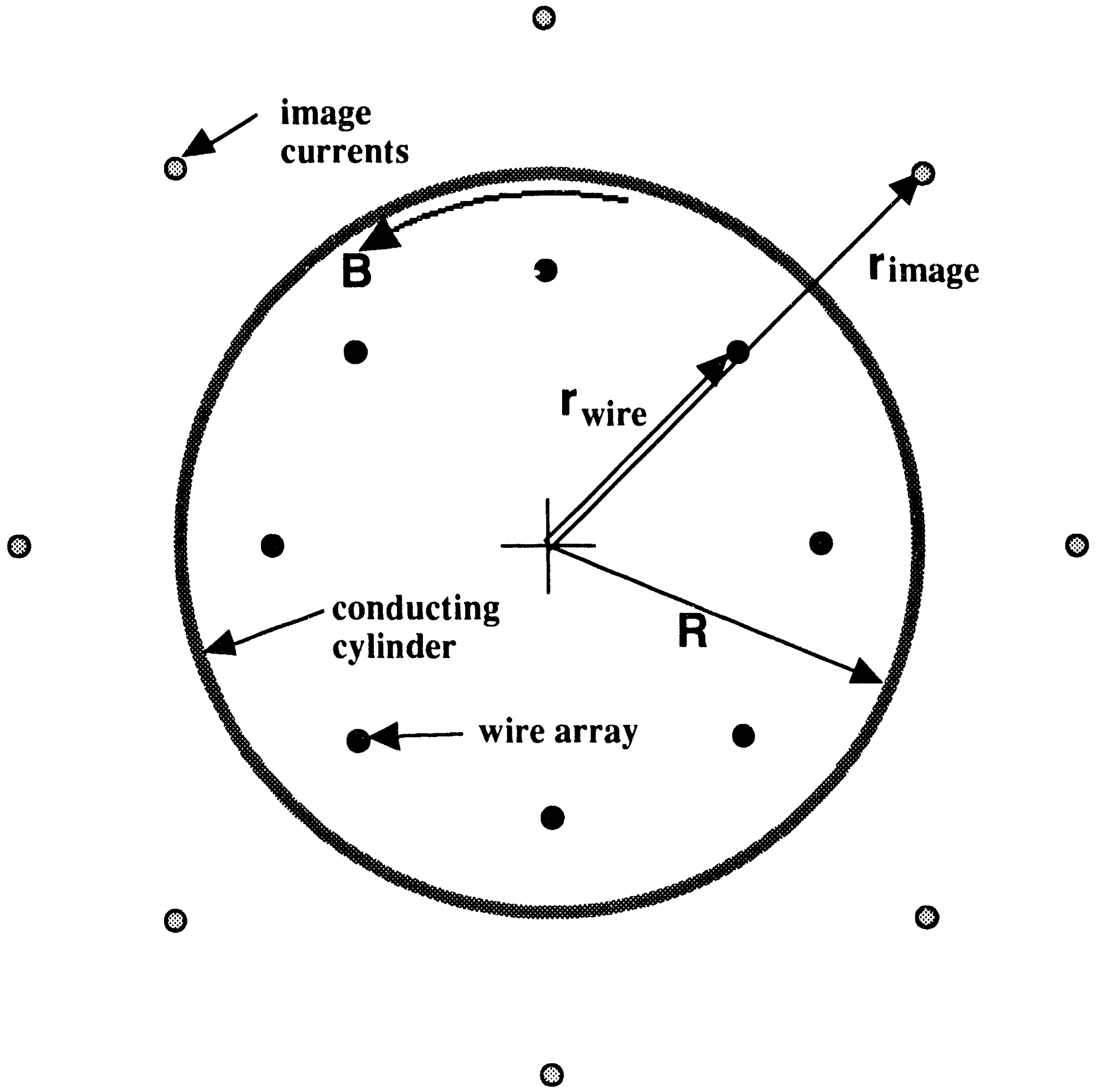

Figure 25. Locations of image currents (shaded) and wire array currents (solid) in a perfectly conducting cylinder. B at the cylinder is entirely azimuthal.

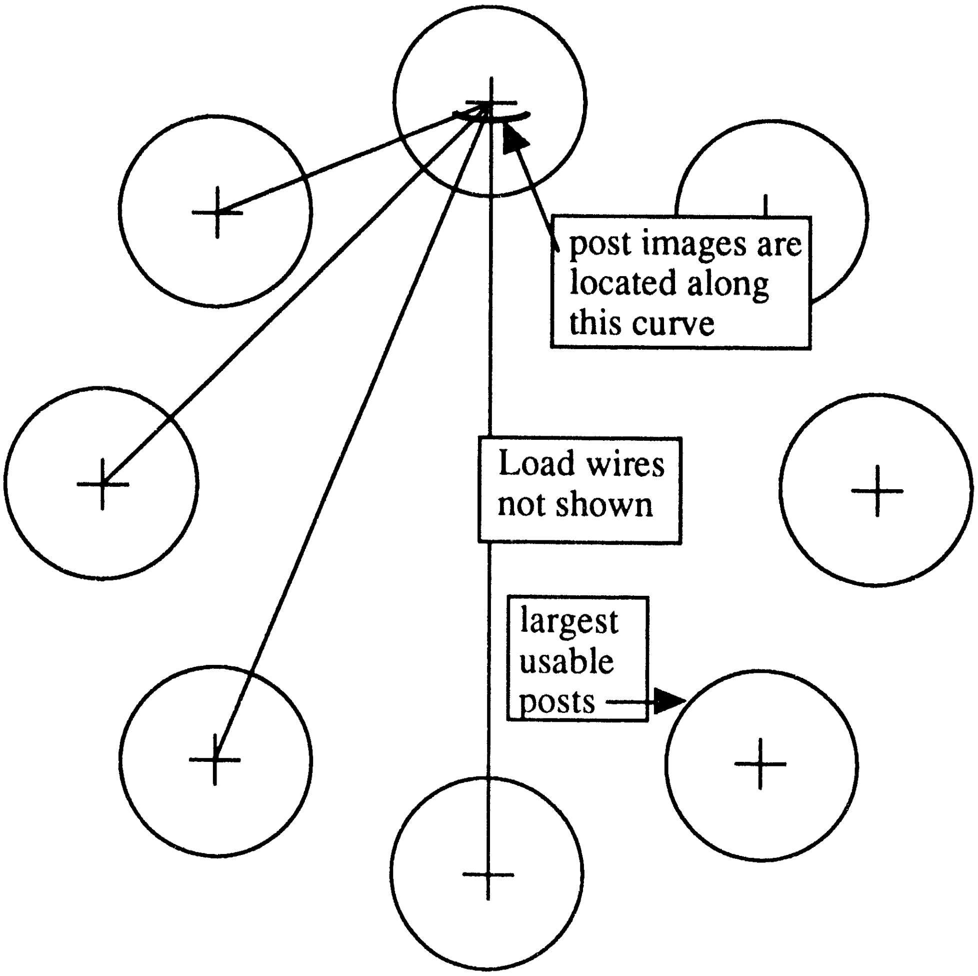

Figure 26. Approximate location of image currents in a post from currents in all other posts. Net effect is a small radially inward movement of the post current.

4. Specific Examples

For a solid outer cylinder radius of 0.6 cm and load wire circle 0.2-cm radius, with array length of 2 cm, the calculated inductances (nH) versus number of wires by the numerical calculation (Lnum) and using the formula from Grover (Lgrov) are:

No. wires	3	6	9	12	15	18	21	24	27	30
Lnum	7.84	5.66	5.06	4.79	4.65	4.57	4.51	4.47	4.45	4.43
Lgrov	9.11	6.29	5.48	5.11	4.91	4.71	4.70	4.64	4.59	4.56

The corresponding inductance of two coaxial cylinders ($R_i = 0.2$ cm, $R_0 = 0.6$ cm) is 4.39 nH. The larger inductance in Lgrov is probably due to the flux allowed in the wires.

Replacing the outer cylinder with 8 posts of 0.25-cm diameter (centers at 0.6-cm radius) produced an inductance of 4.43 nH for a 12-wire array, somewhat less than the inductance of the same wire array with an outer cylinder located at the same radius as the post centers. In this case, flux excluded from the interior of the large posts more than compensates for the flux that leaks to the outside of the post circle.

A second configuration with a solid outer cylinder of radius 1.75 cm and load wire circle radius of 0.75 cm and length of 2 cm produced inductances (nH) vs. wire number as follows:

No. wires	3	6	9	12	15	18	21	24	27	30
Lnum	8.57	5.52	4.63	4.22	3.99	3.85	3.75	3.69	3.63	3.59
Lgrov	9.86	6.16	5.06	4.54	4.26	4.07	3.94	3.85	3.78	3.73

The corresponding coaxial cylinder ($R_i = 0.75$ cm, $R_0 = 1.75$ cm) inductance is 3.39 nH.

An outer conductor of eight , 0.32-cm diameter posts (centers at 1.75-cm radius) in place of the cylinder produced a calculated inductance of 4.48 nH in a 12-wire array. Reducing the post diameter to 0.13 cm increased the inductance to 5.01 nH. These posts are small compared with those in the previous example, and image currents in the posts are completely negligible.

C. Modeling a Z Pinch with Total Immersion PIC

Because of its descriptive nature and agreeable acronym, the term "particle-in-cell," or PIC, has been widely applied to codes which solve the Vlasov equation by computing the trajectories of physical particles. The original PIC code, however, was a fluid code in which particles serve as markers of fluid position and carriers of fluid properties. Like this code, "Total Immersion PIC" (TIP) is a particle-based fluid code based on a new algorithm. TIP mimics fluid behavior by exploiting as much as possible the descriptive power of numerical particles while minimizing the role of the grid. Each particle explicitly exchanges momentum and internal energy with its surroundings in a locally conservative manner consistent with its pressure and environment. Viscosity, heat conduction, and resistivity are handled by using numerical smoothing to simulate physical transport. Except for the vector potential, no partial differential equations are solved on the grid. An important consequence of this is that, although the algorithm is explicit, the maximum stable time step is considerably greater than that of the Courant condition!

TIP is being used to model the z pinch in two versions. The first, in (x,y) geometry, is being used to study the symmetry of implosions produced by conducting post arrays and initial plasma distributions. Figure 27 shows the time evolution of the density for Saturn parameters with 8 posts of 2.9-mm diameter and 20 tungsten wires of 25-µm diameter using the geometry of Fig. 12B. The code in this geometry can follow the magnetic field as it diffuses into the plasma and becomes entrapped within coalescing plasma elements. Several questions will be addressed using (x,y) TIP. The first is the effects of the current carrying posts on the implosion.[17] Clearly, if these posts are too close or if there are too few of them, the symmetry will be adversely affected. The code will be useful in determining when the model proposed by Mosher is applicable. A second question to be examined is the difference in behavior of a pinch when the initial conditions produce a geometry as shown in Fig. 27 versus the case in which the plasma does not form a continuous annulus, but leaves gaps between its elements. In this case, there is a competition between each individual element undergoing its own pinch and the implosion caused by their mutual attraction.

A second version of the code, in (z,r) geometry, will be used to investigate the formation and development of m = 0 instabilities.[26] In particular, the inductive electric field produced by this type of collapse will be examined in an attempt to determine its role in producing local hot spots.

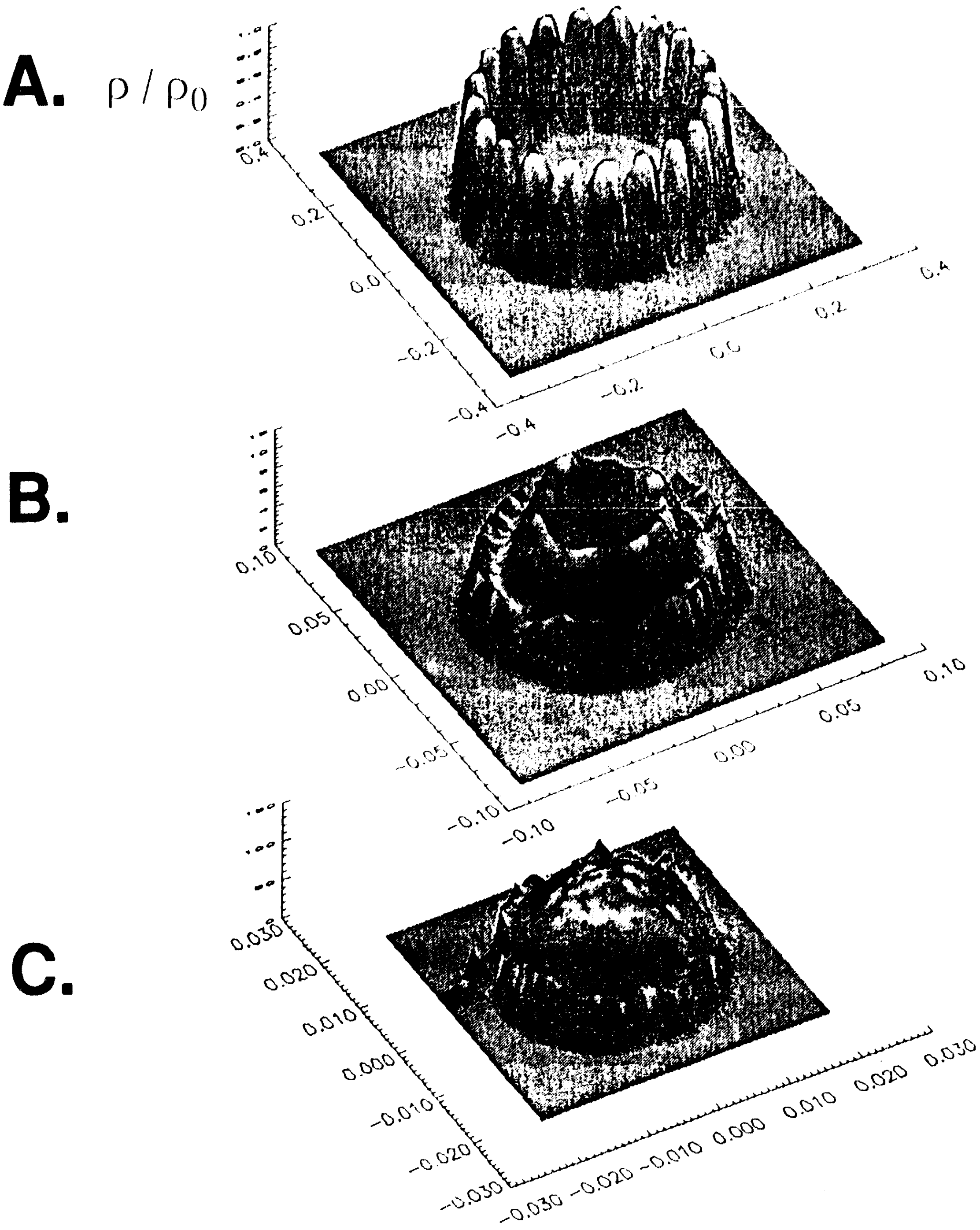

Figure 27. Relative density as a function of position at (A) t = 0 ns, (B) t = 45 ns, and (C) t = 48 ns. Axes are in cm. Peak value of vertical scale is 1, 12, and 150 for Figures A, B, and C, respectively. Configuration corresponds to that of Figs, 2B, 3, and 12A with 2.9-mm diameter posts, twenty 25-μm diameter tungsten wires, $R_i = 2$ mm, and $R_0 = 15.7$ mm.

This page intentionally left blank.

References

1. D. Mosher, "Non-thermal Plasma Radiation Sources for Jupiter White Paper," Jupiter Design Options Study Team Report, January 1994.
2. D. L. Johnson, S. J. Stephanakis, and D. Mosher, NRL Memorandum Report 3207, 1976.
3. P. Spence, Presentation by Physics International Co., Exploding Wire Simulator Application Meeting, Headquarters DNA, October 29-30, 1973.
4. L. M. Choate, "The Saturn X-ray Simulation Facility," Sandia National Laboratories Report, SAND89-1351 (1989).
5. M. J. Clauser, L. Baker, D. H. McDaniel, R. W. Stinnett, and A. J. Toepfer, "Magnetic Implosions of Plasmas with Short Pulse, High Power Generators," Sandia National Laboratories Report, SAND78-1387C (1978).
6. G. B. Zimmerman, "Numerical Simulation of the High Density Approach to Laser-Fusion," Lawrence Livermore Laboratory Preprint UCRL-74811 (October 1973).
7. D. B. Seidel and T. D. Pointon, to be published.
8. J. A. Halbleib, R. P. Kensek, G. D. Valdez, S. M. Seltzer, and M. J. Berger, "ITS: The Integrated TIGER Series of Electron/Photon Transport Codes—Version 3.0," *IEEE Trans. Nucl. Sci.* **39**, 1025 (1992).
9. J. A. Halbleib, "Structure and Operation of the ITS Code System" and "Applications of the ITS Codes," *Monte Carlo Transport of Electrons and Photons*, ed. T. M. Jenkens, W. R. Nelson, and A. Rindi (Plenum Publishing Corporation, (1988), pp. 249-284.
10. R. B. Spielman, private communication, Sandia National Laboratories (November 1993).
11. J. C. Martin, "Fast Pulse Vacuum Flashover," AWRE Report SSWA/JCM/713/157, Atomic Weapons Research Establishment, Aldermaston, England (1971).
12. J. P. VanDevender, D. H. McDaniel, E. L. Neau, R. E. Mattis, and K. D. Bergeron, "Magnetic Inhibition of Insulator Flashover," *J. Appl. Phys.* **53**, 4441 (1982).
13. T. H. Martin and D. H. McDaniel, private communication, Sandia National Laboratories (December 1993).
14. D. Mosher, S. J. Stephanakis, K. Hain, C. M. Dozier, and F. C. Young, "Electrical Characteristics of High Energy-Density Exploding Wire Plasmas," *Annals of the New York Academy of Science* **251**, 632 (May 8, 1975).
15. R. Humphreys, "Optimum Inductance Change in a Z-Pinch," Internal Sandia National Laboratories Memo to K. Matzen (April 8, 1993).

16. R. B. Spielman, J. L. Porter, and M. A. Hedemann, "Wire Array Z-Pinch Experiments on Saturn," Sandia National Laboratories Report (to be published 1994).

17. D. Mosher, "Plasma Radiation Source Implosion Limit Due to Azimuthal Asymmetries," submitted to the 10th International Conference on High-Power Particle Beams (June 20-24, 1994), San Diego, CA.

18. B. M. Marder, "Total Immersion PIC," submitted to *Comp. Phys. Comm.* (April 1994).

19. B. Goplin, R. E. Clark, J. McDonald, W. M. Bollen, "Users Manual for MAGIC," Mission Research Corporation Report No. MRC/WDC-R-068, Alexandria, VA, September 1983.

20. Herman Kahn, "Applications of Monte Carlo," RM-1237-AEC, 19 April 1954 (Revised 27 April 1956).

21. T. W. L. Sanford, J. A. Halbleib, J. W. Poukey, A. L. Pregenzer, R. C. Pate, C. E. Heath, R. Mock, G. A. Mastin, D. C. Ghiglia, T. J. Roemer, P. W. Spence, and G. A. Proulx, "Measurement of Electron Energy Deposition Necessary to Form an Anode Plasma in Ta, Ti, and C for Coaxial Bremsstrahlung Diodes," *J. Appl. Phys.* **66**, 10 (1989).

22. V. Bailey, Pulsed Sciences Incorporated. private communication (1991).

23. B. B. Godfrey and D. R. Welch, 12th Conference on Numerical Simulations of Plasmas, San Francisco, CA, 1987.

24. The MathWorks, Inc. Cochituate Place, 24 Prime Park Way, Natick, MA 01760, phone: 508-653-1415, fax: 508-653-2997.

25. Grover, F. W., *Inductance Calculations*, Dover Publications, Inc., New York, 1962.

26. D. Mosher and D. Colombant, "Pinch Spot Formation in High Atomic Numer Z Discharges," *Phys. Rev. Letts.* **68**, 2600 (1992).

Distribution

2 University of New Mexico
Dept. of Chemistry & Nuclear Eng.
Attn: Prof. G. Cooper
Prof. S. Humphries
Albuquerque, NM 87131

2 Ktech Corp.
Attn: T. Smith
T. Roemer
901 Pennsylvania NE
Albuquerque, NM 87110

6 Los Alamos National Laboratory
Attn: T. Kozlowski
R. J. Macek
R. Stringfield
H. A. Thiessen
G. Idzorck
R. Bartlett
P. O. Box 1663
Los Alamos, NM 87545

1 W. J. Schafer Assoc., Inc.
Attn: D. C. Straw
2000 Randolph Road SE, Suite 205
Albuquerque, NM 87106

1 Mission Research Corporation
Attn: D. R. Welch
1720 Randolph Road SE
Albuquerque, NM 87106

1 North Star Research Corp.
Attn: R. J. Adler
5555 Zuni SE, Suite 345
Albuquerque, NM 87108

1 Titan Industries
Attn: R. B. Miller
P. O. Box 9254
Albuquerque, NM 87119

4 Fermilab
Attn: Prof. L. M. Lederman,
Director Emeritus
J. H. Christenson
H. B. Jensen
T. E. Nash
P. O. Box 500
Batavia, IL 60510

1 University of California Davis
Attn: Prof. John deGroot
Department of Applied Science
228 Walker Hall
Davis, CA 95616

7 Harry Diamond Laboratories
Aurora Facility
Attn: J. Corrigan, Director
M. Bushell
R. Fleetwood
K. G. Kerris
J. McGarrity
G. Merkel
M. Smith
2800 Powder Mill Road
Adelphi, MD 20783

1 Center for Radiation Research
Attn: S. M. Seltzer
National Bureau of Standards
Gaithersburg, MD 20899

7 Naval Research Laboratory
Attn: G. Cooperstein
D. Hinshelwood
D. Mosher
J. M. Neri
P. Ottinger
F. C. Young
R. Commisso
Washington, DC 20375

1 Stanford Linear Accelerator Center
Attn: W. R. Nelson
P. O. Box 4349
Stanford, CA 94305

1 Air Force Institute of Technology
Dept. of Engineering Physics
Attn: Prof. D. E. Beller
Wright-Patterson AFB, OH
45433-6583

1 Auburn University
Office of the Vice President for
Research
Attn: Prof. A. K. Hyder
Associate Vice President
202 Samford Hall
Auburn, AL 36849-5112

Distribution (continued)

1 Columbia University
Physics Department
Attn: Prof. W. Lee
538 W. 120 Street
New York, NY 10027

2 Cornell University
Laboratory of Plasma Sciences
Attn: Prof. J. B. Greenly
Prof. D. A. Hammer
369 Upson Hall
Ithaca, NY 14853-7501

1 Massachusetts Institute of Technology
Plasma Fusion Center
Attn: Prof. R. D. Petrasso
167 Albany St.
Cambridge, MA 01239

1 George Washington University
Department of Physics
Attn: Prof. B. L. Berman
211 Samson Hall
Washington, DC 20052

1 New York University
Physics Department
Attn: Prof. J. Sculli
4 Washington Place
New York, NY 10003

1 University of Maryland
Laboratory for Plasma and Fusion Energy Studies
Attn: Prof. Moon-Jhong Rhee
College Park, MD 20742

2 Berkeley Research Associates
Attn: N. R. Pereira
J. Golden
P. O. Box 852
Springfield, VA 22150

1 Mission Research Corporation
Attn: V. A. J. van Lint
P. O. Drawer 719
Santa Barbara, CA 03102

6 Physics International Co.
Attn: H. Helava
J. Creedon
C. Gilman
Sik-Lam Wong
J. C. Riordan
P. Sincerny
2700 Merced Street
San Leandro, Ca 94577

4 Pulse Science Inc.
Attn: V. Bailey
I. Smith
J. Fockler
P. Spence
600 McCormick St.
San Leandro, CA 94577

3 Science Applications, Inc.
Attn: A. A. Mondelli
D. Bacon
A. Manofsky
1710 Goodridge Drive
P. O. Box 1303
McLean, VA 22101

1 Lawrence Livermore National Laboratory
Attn: P. Springer
P. O. Box 808
Livermore, CA 94550

5 Atomic Weapons Research Establishment
Attn: N. Fenner
M. Gunerson
B. Harris
J. C. Martin
G. Wilson
Aldermaston, Reading RG7 4PR
Berkshire
ENGLAND

1 Culham Laboratory
Culham Lightning Studies Unit
Attn: C. J. Hardwick
Abingdon, Oxfordshire OX14 3DB
ENGLAND

Distribution (continued)

3 Rutherford Appleton Laboratory
Attn: T. G. Walker, Dep. Director
T. Broome
C. Damerell
Chilton, Didcot
Oxon. OX11 OQx
ENGLAND

1 University des Sciences et
Techniques du Languedoc
Centre d'Electronique de Montpellier
Attn: Prof. J. Gasiot
Place E. Battaillon
F-34 060 Montpellier Cedex
FRANCE

4 Kernforshungszentrum Karlsruhe Gmbh.
Attn: W. Bauer
H. Bluhm
P. Hoppe
H. U. Karow
Postfach 3640, D-7500 Karlsruhe 1
FEDERAL REPUBLIC OF GERMANY

6 C. E. R. N.
CH-1211
Attn: W. Blum
V. Chabaud
G. Jarlskog
G. Lutz
W. Manner
P. Weilhammer
Geneva 23
SWITZERLAND

1	MS 0360	A.R.C. Westwood, 1000
1	MS 0352	M. J. Clauser. 1001
1	MS 0335	F. L. Vook, 1100
1	MS 1190	D. L. Cook, 1200
1	MS 1195	J. P. Quintenz, 1202
1	MS 1181	K. R. Prestwich, 1203
1	MS 1178	J. J. Ramirez, 1204
1	MS 1182	R. W. Stinnett, 1205
1	MS 1187	T. A. Mehlhorn, 1207
1	MS 1181	J. M. Hoffman, 1208
1	MS 1193	T. H. Martin, 1211
1	MS 1178	R. Hamil, 1212
1	MS 1178	J. P. Corley, 1212
1	MS 1178	S. Drennan, 1212
1	MS 1182	B. N. Turman, 1221
1	MS 1193	J. E. Maenchen, 1231
1	MS 1193	M. E. Cuneo, 1231
1	MS 1193	W. E. Fowler, 1231
1	MS 1193	D. L. Hanson, 1231
1	MS 1193	D. J. Johnson, 1231
1	MS 1193	M. G. Mazarakis, 1231
1	MS 1193	P. R. Menge, 1231
1	MS 1193	R. C. Mock, 1231
1	MS 1193	T. J. Renk, 1231
1	MS 1193	D. C. Rovang, 1231
15	MS 1193	T. W. L. Sanford, 1231
1	MS 1193	D. D. Bloomquist, 1236
1	MS 1184	J. Boyes, 1239
1	MS 1186	C. L. Olson, 1241
1	MS 1186	J. W. Poukey, 1241
1	MS 1186	S. E. Rosenthal, 1241
1	MS 1186	M. A. Sweeney, 1241
1	MS 1186	B. D. Marder, 1241
1	MS 1186	D. B. Seidel, 1242
1	MS 1152	D. L. Johnson, 1243
1	MS 1152	E. L. Neau, 1243
1	MS 1153	M. T. Buttram, 1248
1	MS 1187	G. A. Allshouse, 1271
1	MS 1187	M. K. Matzen, 1271
1	MS 1187	D. R. Humphreys, 1271
1	MS 1187	E. McGuire, 1271
1	MS 1187	R. Olson, 1271
1	MS 1194	D. H. McDaniel, 1273
1	MS 1194	C. W. Mendel, 1273
1	MS 1194	G. Rochau, 1273
1	MS 1194	S. M. Cameron, 1273
1	MS 1194	J. T. Crow, 1273
1	MS 1194	W. Moore, 1273
1	MS 1194	T. Nash, 1273
1	MS 1194	J. Porter, 1273
1	MS 1194	M. Savage, 1273
1	MS 1194	J. Seamen, 1273
1	MS 1194	R. B. Spielman, 1273
1	MS 1194	S. Breeze, 1273
1	MS 1194	T. Gilliland, 1273
1	MS 1194	D. Jobe, 1273
1	MS 1194	J. McGurn, 1273
1	MS 1194	L. Ruggles, 1273
1	MS 1194	D. Sparks, 1273
1	MS 1194	K. Struve, 1273
1	MS 1194	M. Vargas, 1273
1	MS 1194	K. Ward, 1273
1	MS 1105	R. J. Leeper, 1277
1	MS 1105	D. L. Fehl, 1277
1	MS 1105	T. R. Lockner, 1277
1	MS 1105	W. A. Stygar, 1277
1	MS 1105	C. L. Ruiz, 1277
1	MS 0321	E. H. Barsis, 1400

Distribution (continued)

1	MS 0336	R. J. Eagan, 1700
1	MS 1188	F. McNamara, 1815
1	MS 0952	D. J. Miller, 2161
1	MS 1369	J. P. VanDevender, 4700
1	MS 0463	R. L. Hagengruber, 5000
1	MS 0479	L. M. Choate, 5151
1	MS 1143	J. K. Rice, 6500
1	MS 1141	T. R. Schmidt, 6502
1	MS 1145	R. J. Lipinski, 6514
1	MS 1145	R. L. Coats, 6514
1	MS 1183	K. W. Hanks, 6911
1	MS 0151	G. Yonas, 9000
1	MS 1165	J. E. Powell, 9300
1	MS 1165	P. S. Raglin, 9300
1	MS 1158	J. D. Plimpton, 9301
1	MS 1170	G. A. Zawadzkas, 9302
1	MS 1155	W. Beezhold, 9303
1	MS 1170	M. J. Navratil, 9305
1	MS 1160	F. Biggs, 9312
1	MS 1160	G. J. Lockwood, 9312
1	MS 1160	J. Schwarz, 9312
1	MS 1179	W. P. Ballard, 9341
1	MS 1179	D. E. Beutler, 9341
1	MS 1179	R. S. Klingler, 9341
1	MS 1179	N. E. Counts, 9341
1	MS 1179	R. E. Craven, 9341
1	MS 1179	J. A. Halbleib, 9341
1	MS 1179	M. A. Hedemann, 9341
1	MS 1179	R. P. Kensek, 9341
1	MS 1179	J. R. Lee, 9341
1	MS 1179	L. J. Lorence, 9341
1	MS 1179	T. F. Wrobel, 9341
1	MS 1106	J. P. Reilly, 9342
1	MS 1106	A. W. Sharpe, 9342
1	MS 1106	R. Pepping, 9342
1	MS 1106	B. Peyton, 9342
1	MS 1106	P. Reilly, 9342
1	MS 1106	R. Broyles, 9342
1	MS 1106	B. Henderson, 9342
1	MS 1166	J. H. Renken, 9352
5	MS 0899	Technical Library, 7141
1	MS 0619	Tech. Publications, 7151
10	MS 0100	Document Processing for DOE/OSTI, 7613-2
1	MS 9018	CTF, 8523-2

DATE

FILMED

7/7/94

END